

**Automation of a broadband infrared hyperspectroscopy
apparatus**

by

Robyn McNeil

B.A.Sc., University of Toronto, 2019

A THESIS SUBMITTED IN PARTIAL FULFILLMENT
OF THE REQUIREMENTS FOR THE DEGREE OF

Master of Applied Science

in

THE FACULTY OF GRADUATE AND POSTDOCTORAL
STUDIES

(Electrical and Computer Engineering)

The University of British Columbia
(Vancouver)

August 2021

© Robyn McNeil, 2021

The following individuals certify that they have read, and recommend to the Faculty of Graduate and Postdoctoral Studies for acceptance, the thesis entitled:

Automation of a broadband infrared hyperspectroscopy apparatus

submitted by **Robyn McNeil** in partial fulfillment of the requirements for the degree of **Master of Applied Science in Electrical and Computer Engineering**.

Examining Committee:

Alireza Nojeh, Department of Electrical and Computer Engineering
Supervisor

Jeff Young, Department of Physics and Astronomy
Examining Committee Member

Abstract

The purpose of this study was to improve upon the design of a high-spatial-resolution broadband hyperspectroscopy system primarily by building a full-stack automation software. This apparatus provides optical heating to a sample and collects the resulting incandescent image of the surface with a high spacial resolution using a Fourier Transform Infrared (FTIR) spectrometer.

The function of each component of the system was reviewed including the incident beam and associated focusing optics, the vacuum chamber and sample mounting platform, the infrared image collection optics and the FTIR spectrometer which detects the signal. The Gaussian optics physics which dictate the incident excitation beam were reviewed and applied to a Zemax Opticstudio [1] simulation which demonstrated the alignment constraints and function of each optical component. A similar Opticstudio simulation was constructed to define the outgoing signal, and an alignment procedure was derived and demonstrated for both the incoming and outgoing signal. The function and configuration of the FTIR spectrometer was reviewed and a Computer Aided Design (CAD) model of the entire system was built in Solidworks [2].

A full-stack automation software called HypIR was built which included a back-end written in C to facilitate device coordination and control, a front-end written with the Tkinter Python library [3] to facilitate user interface and an SQL database [4] to maintain all experimental parameters. A simulated Infrared (IR) image was produced using a high intensity fibre light source which was directed through the optics and the spectrometer to produce hyperspectra via the HypIR software. A post-processing procedure was constructed which fits the data to black-body radiation to extract a temperature map, confirming the functionality of the

software. This software and process can be used in the future to more effectively and efficiently collect hyperspectra, which will provide the data needed to understand novel thermal emission behaviour in materials.

Lay Summary

The primary purpose of this work was to design and build a piece of software which would allow a user to interact with and run a complex measurement instrument. This instrument uses light to interact with materials, uses an optical system to collect infrared light that is emitted by the sample, then feeds that light to a spectral measurement device. The optical and mechanical components were simulated in software and some components were modified such as the chamber where the sample is held in a specific environment. The software was proven to execute the functionality of the instrument effectively. A computer model was built of the entire system, and simulations were carried out to track the light travelling through the system.

Preface

This dissertation is based on a hyperspectroscopy system developed by A. Nojeh, M. Chowdhury and H. Fan. The concept, design and initial prototype of the device were completed by these colleagues in previous works (mostly unpublished, except for aspects of a preliminary, early version [5]).

The software component, simulations, CAD renderings, results and hardware modification included herein were completed by the author R. McNeil under the supervision and technical guidance of A. Nojeh.

Table of Contents

Abstract	iii
Lay Summary	v
Preface	vi
Table of Contents	vii
List of Tables	ix
List of Figures	x
Glossary	xv
Acknowledgments	xvi
Dedication	xvii
1 Introduction	1
2 Opto-Mechanical System Design	7
2.1 Incident Optical Excitation Beam	7
2.1.1 Gaussian Beam Propagation	7
2.1.2 Beam Focusing via Objective Lens	10
2.1.3 Spot Size Control and Optimization	13
2.2 Ultra-High Vacuum Chamber Design	16
2.3 Design of Hyperspectroscopy Opto-Mechanics	20

2.3.1	Simulation of Infrared Signal Collection and Propagation .	20
2.3.2	Global Calibration Source Alignment	23
2.3.3	Visible Source Alignment	26
2.3.4	Fourier Transform Infrared Spectroscopy Spectra Collection	28
3	Automation Software Design	30
3.1	Program Initialization	30
3.2	Opening Page	32
3.3	Linear Stage Control Page	33
3.4	Optical Setup Page	34
3.5	Parameter Window	35
3.6	Data Retrieval	38
3.7	Scan Execution	38
4	Results and Discussion	40
4.1	Scan Procedure	40
4.2	Device Calibration	42
4.3	Temperature Extraction	43
4.4	Results	44
4.5	Material Parameter Extraction	48
5	Conclusions and Future Work	49
5.1	Summary and Conclusions	49
5.2	Future Work	51
	Bibliography	52

List of Tables

Table 2.1	Verdi V-5 Laser Output Specifications [6]	8
Table 2.2	CCD Camera + Zoom System Specifications [7][8]	16
Table 2.3	Optimized Optical Setup Parameters	24

List of Figures

Figure 1.1	A diagram of varying carbon nanotube configurations including a single wall (black), double walled (blue), and triple walled (green) [9]	2
Figure 1.2	a) Photo of 1.5 mm tall carbon nanotube forest grown on a silicon wafer, inset being a scanning electron micrograph showing vertical alignment [10]. Scale bars are 1 mm (photo) and 1 μm (inset) b) upon excitation with a 250 μm wide optical beam (filtered from image), the Carbon Nanotube Forest (CNTF) visibly displays the incandescent spot from the confined heated region [10]. Reprinted figure with permission from [Mike Chang, Harrison D. E. Fan, Mokter M. Chowdhury, George A. Sawatzky, and Alireza Nojeh, Physical Review B, 98, 155422, 2 2018] Copyright 2018 by the American Physical Society.	3
Figure 1.3	A block diagram of the primary components of the hyperspectrometer. The incoming signal is focused with a biconvex lens, passes through a beamsplitter, is focused by an objective lens and hits the sample in a Ultra-High Vacuum (UHV) chamber. The outgoing incandescent signal is magnified by the objective, is reflected by the beamsplitter, is moved using the translational optics and is scanned by the spectrometer.	6

Figure 2.1	CAD rendering of the incident beam path from the laser, around unrelated equipment in its path, through the beam splitter, through the objective lens and onto the sample in the UHV chamber . .	8
Figure 2.2	Schematic of Gaussian beam propagation [11]	10
Figure 2.3	Beam waist defined as Surface 1, distance from the waist to the laser output port is optimized to have a beam diameter of 2.25 mm as described by the manufacturer. This results in a distance of 2035.548 mm.	11
Figure 2.4	Schematic of beam tracing through objective lens from right to left [12]	11
Figure 2.5	CAD rendering of objective lens assembly	12
Figure 2.6	CAD rendering of UHV view-port in line with objective lens .	12
Figure 2.7	Zemax rendering of objective lens ray tracing from left to right with an incoming beam diameter of 4 mm. With this diameter, the beam would reach the sample surface after passing through the viewport.	14
Figure 2.8	Zemax rendering of objective lens ray tracing from left to right with an incoming beam diameter of 2.25 mm. The beam is refracted by the second mirror back through the hole in the first mirror which it emerged from, rather than being refracted by said mirror back towards the sample.	14
Figure 2.9	Zemax rendering of bi-convex lens implementation. Laser beam is incoming from the left to a) the bi-convex lens, through b) the objective lens, through c) the viewport and finally to d) the beam terminating at the sample surface. The resulting spot rendering is shown on the right.	15
Figure 2.10	CAD schematic of optical setup for in-situ imaging camera. The camera is mounted on micro-adjusters for fine positional adjustment and placed at the working distance of the camera to begin the focusing process.	17
Figure 2.11	Image collected by focusing the in-situ camera on the sample surface	17

Figure 2.12	CAD rendering of biconvex lens setup on optical table. The lens is initially placed at 500mm from the objective lens as per the simulations, and finely adjusted using the micro-adjuster stages.	18
Figure 2.13	Spot size adjustment via axial shifting of biconvex lens with approximately 53% laser power reaching the sample	18
Figure 2.14	CAD schematic of UHV chamber including a) a turbo pump b) a connection to dry scroll pump c) a blank flange d) a ZnSe viewport e) a mounting plate f) a connection point for a cold cathode gauge g) a future electronics access point h) a rear viewport i) a pirani gauge j) a top viewport	19
Figure 2.15	CAD schematic of sample stage and mounting device for CNTF	20
Figure 2.16	CAD rendering of the outgoing image path a) through the objective lens b) reflected by the beamsplitter c) reflected upwards by the parascopic mirrors d) reflected through the translational optics e) collected by the spectrometer. The inset image depicts the beam path through the parascopic mirrors and the translational optics.	21
Figure 2.17	Zemax ray tracing demonstrating ray block at objective lens when objective is configured as defined by Section 2.1.3 . . .	22
Figure 2.18	Corroborating zemax simulations for the incoming signal (a), a 100 μm laser spot (b), the outgoing signal (c) and a focused image at the FTIR entrance port (d). The image used is the default test image found in Zemax Opticstudio.	23
Figure 2.19	Demonstration of depth of focus with regards to the objective lens and spectrometer positioning. Changing the position of the objective lens will have a much larger impact on the image focus than changing the distance from the object to the spectrometer	23
Figure 2.20	Emission spectrum of Globar IR source	25
Figure 2.21	CAD rendering of 100 μm aperture mounted to vacuum chamber	25

Figure 2.22	Schematic showing alignment two step procedure where a laser (green line) is aligned to the hot spot and alignment apertures are placed on the table (a) which are then used to align the optics with the infrared signal (red line) (b)	26
Figure 2.23	Alignment procedure with laser pointer and 100 μm illuminated aperture	26
Figure 2.24	CAD rendering of IR camera alignment. If distance A equals distance B, than a focused image at the IR camera would be focused at the spectrometer entrance port once the rotating mirror is shifted between path A and B.	27
Figure 2.25	Fiber light source mounted directly in front of the motorized mirrors fitted with steel tube to increase signal power	28
Figure 2.26	Beam path within FTIR spectrometer with emission entering through the exterior entrance port and interferometer schematic	29
Figure 3.1	Block diagram representation of full-stack HypIR software including communication channel protocols	31
Figure 3.2	Select the control.exe executable through the OPUS External Program function	32
Figure 3.3	Welcome page of HypIR software	33
Figure 3.4	Stage control page	34
Figure 3.5	Stage error message	34
Figure 3.6	Optical setup input page	35
Figure 3.7	Scan parameter input page	36
Figure 3.8	Error messages	36
Figure 3.9	Check with user for background scan	37
Figure 3.10	Scan procedure schematic	37
Figure 3.11	Check with user for sample scan	37
Figure 4.1	Background real time spectra capture in OPUS software	41
Figure 4.2	IR signal confirmed with real time spectra capture	41

Figure 4.3	Normalized Near Infrared (NIR) reference spectrum (blue), Normalized energy radiance at 2059.4765 K (red), Normalized final calibration curve (black)	43
Figure 4.4	Poor curve fitting, but proportional intensity to spot location	45
Figure 4.5	Increasing resolution from a)5x5 b)7x7 c)11x11	46
Figure 4.6	Change in IR signal when source was switched between a) half power and b) full power	46
Figure 4.7	Approximately 2 cm translation of image a)down and c)up corresponding to 2 cm stage translation. Distortion in figure c) corresponds to signal dispersion due to lack of image focus	47
Figure 5.1	Flow schematic for design process and project progress	50

Glossary

This glossary contains a list of common acronyms and their associated phrases used throughout this dissertation.

CAD	Computer Aided Design
CNT	Carbon Nanotube
CNTF	Carbon Nanotube Forest
CNTS	Carbon Nanotubes
DOF	Depth of Field
FOV	Field of View
FTIR	Fourier Transform Infrared
IR	Infrared
NA	Numerical Aperture
NIR	Near Infrared
UHV	Ultra-High Vacuum
WD	Working Distance

Acknowledgments

I would like to sincerely thank my colleagues in the Nanostructures Group and the Stuart Blusson Quantum Matter Institute for selflessly providing invaluable resources and mentorship throughout my work.

I would like to especially thank my supervisor Professor Alireza Nojeh for his feedback, guidance and patience throughout this project. Even as a global pandemic made his job exponentially harder, Professor Nojeh always took the time to ensure my progress and remained patient and considerate in all of our interactions.

Lastly, I would like to express my sincere gratitude to the UBC Skatepark and the Vancouver Skateboarding community for remaining a source of joy and perspective throughout these difficult two years.

Dedication

I would like to dedicate this work to my gran, Catherine Malone. Without her generosity I would not have been able to begin graduate studies, never mind finish them. A brilliant scientist, a loving grandmother and an extraordinary quilter, she has always been one of my greatest role models. Thank you for always being there for me, and for showing a little girl that one day she could grow up to be a scientist too.

Chapter 1

Introduction

In the last two decades, nanomaterials and nanostructures have increasingly been pursued as solutions to fundamental engineering problems. The quantum effects introduced by their reduced dimensionality often result in novel physical behaviour which can be exploited to surpass the performance of macroscopic alternatives.

An example of one of these structures which exhibit promising physical properties are Carbon Nanotubes (CNTs). These are a class of material which describe one or more concentric layers of the graphene structure formed into a cylinder as shown in Figure 1.1 [9, 13]. These tubes have a diameter of 100 nm or less and macroscopic long range order along their length which classifies them as quasi one-dimensional nanostructures [10]. Depending on their lattice configuration and diameter, they can exhibit a range of promising characteristics such as high electronic conductivity, high thermal conductivity, high aspect ratio, high surface-to-volume ratio and high mechanical strength to weight ratio.

Carbon nanotubes can be formed into a variety of configurations and bulk structures which exhibit unusual characteristics due to the complex coupling of the anisotropic behaviour between tubes. An example of one of these configurations which exhibit surprising effects is the Carbon Nanotube Forest (CNTF) which is an array of vertically aligned conductive nanotubes as depicted in Figure 1.2 a). One of the most well known properties of this material is its interaction with light. Specifically a forest of single walled carbon nanotubes (SWCNTs) has been reported to be the material which behaves most similarly to a black body radiator

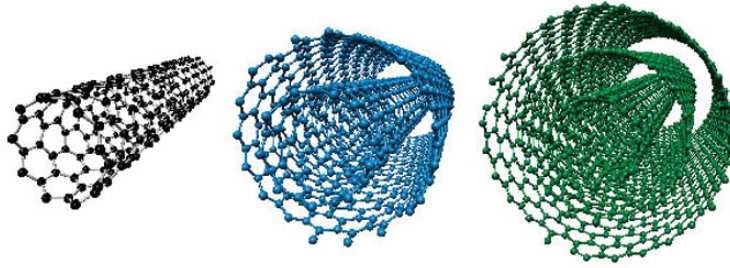


Figure 1.1: A diagram of varying carbon nanotube configurations including a single wall (black), double walled (blue), and triple walled (green) [9]

[14].

A black body radiator describes a theoretical body which absorbs all light of any wavelength which falls on it, with no transmission or reflection [14]. Since no visible light is reflected from the material, it would appear completely dark, hence the “black” body naming. This material also describes the theoretical limit for thermal absorption and emission as, at thermal equilibrium, all light which is not transmitted or reflected is equally absorbed and emitted at every wavelength [14]. The emissivity of a SWCNT forest which describes the ratio of its thermal emission to a black body at the same temperature has been reported as the highest of any material at 0.98–0.99 over a spectral range of 5–12 μm , and its reflectance 0.01–0.02 over a spectral range of 0.2–200 μm [14]. This bulk behaviour may be thought of as all of the reflection/transmission events taking place at each tube leading to absorption by the neighbouring tubes, resulting in a bulk absorption of almost all incident radiation [10].

CNTFs have also been reported to exhibit extreme heat localization upon being illuminated with an incident visible laser beam; called the “heat trap effect” [10, 15]. A high ratio between the thermal conductivity along the axis of CNTs and the transverse direction has been reported [10], which is consistent with relative localization perpendicular to the tube axis. However, optically generated heat has been shown to be tightly confined to the incident laser spot in both directions [10, 15], contradicting the high thermal conductivity along the axis.

This effect is demonstrated in Figure 1.2 b) [10], where the visible beam is filtered out of the image such that only the tightly confined incandescent spot due

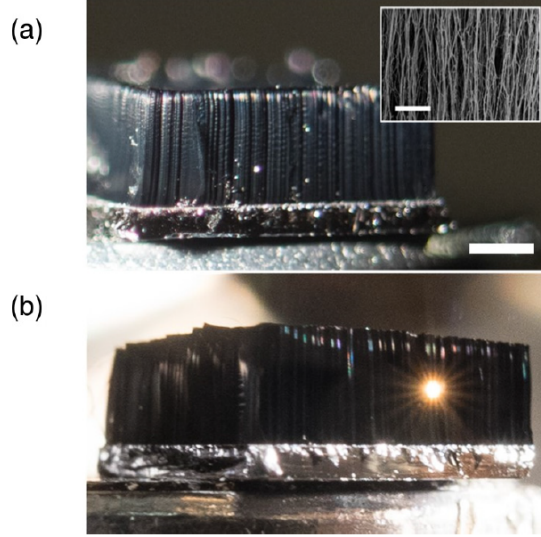


Figure 1.2: a) Photo of 1.5 mm tall carbon nanotube forest grown on a silicon wafer, inset being a scanning electron micrograph showing vertical alignment [10]. Scale bars are 1 mm (photo) and 1 μm (inset) b) upon excitation with a 250 μm wide optical beam (filtered from image), the CNTF visibly displays the incandescent spot from the confined heated region [10]. Reprinted figure with permission from [Mike Chang, Harrison D. E. Fan, Mokter M. Chowdhury, George A. Sawatzky, and Alireza Nojeh, Physical Review B, 98, 155422, 2 2018] Copyright 2018 by the American Physical Society.

to heat localization is shown. This confinement results in peak temperatures of over 2000 K at the center of this incandescent spot, which is excited by tens of milliwatts. This temperature provides the thermal energy to induce thermionic emission and multiphoton photo-electron emission [16], which can be applied to devices such as thermionic energy converters [17]. This is in contrast to classical conductors which require around three orders of magnitude higher irradiance to reach the same temperature [10].

A study was completed which treated the CNTF as a bulk material with the incandescent spot as following Planck's law due to the black body behaviour described above. The study assumed varying degrees of anisotropy, material dimen-

sionality and thermal conductivity temperature dependence in order to fit the heat localization and steep temperature gradient observed in experiment [5, 10] to an associated model of thermal conductivity and emissivity. This study determined that the material dimensionality and anisotropy as well as a reduction in thermal conductivity as temperature increases could result in the heat trap effect found in experiment [10].

However, there still exists a need to accurately map the temperature distribution on the hot spot, to corroborate this model with experimental results, to confirm/deny the assumptions held in the model and to map novel spectral/spatial emission effects in other materials in the future. Previous work in our group has accomplished the mapping of temperature and IR spectra with a hyperspectrometer, but this device lacks the ease of use and robust automation necessary for a higher experimental throughput. If the model described above is correct, then it may follow that regardless of their bulk conductivity, the planar heat confinement, steep temperature increase due to this localized heating and subsequent drop in axial thermal conductivity could be exploited by forming other materials into this quasi one-dimensional forest [10].

An instrument which can extract spatially and spectrally resolved information on this effect is the subject of this dissertation. As shown in Figure 1.3, this device uses a visible laser, a biconvex lens and an objective lens to create an incandescent spot on a Carbon Nanotube (CNT) surface inside a vacuum chamber. The Infrared (IR) image of this spot is magnified by the objective lens, is reflected off of a beam splitter (which the visible signal passes through) and is passed to a set of horizontal and vertical linear stages. As these stages move incrementally, they are used to scan the image across the entrance port of a Fourier Transform Infrared (FTIR) spectrometer which takes scans at each grid point. This produces a grid of spectra representing the incandescent emission across the surface of the sample. These emission spectra can be fitted with Planck curves to determine the temperature at each point, as well as any deviations the spectra may have from Planck radiation. This device was built and proven to work in detecting and mapping the CNT hot spot by other colleagues [5].

The combination of the high magnification of the incandescent image (greater than 150x) and the sub micron resolution of the linear stages leads to the extremely

high spatial resolution which is needed to extract the exact profile of the temperature gradient. As full spectral data are also collected at each of these points, any deviations from thermal equilibrium black body radiation can be tightly correlated to changes in this temperature gradient. This results in a single method to characterize heat localization and the subsequent emission effects.

As is often the case with highly resolved, multi-dimensional characterization devices, the instrumentation is complex and comes with a variety of design challenges. As the incident excitation beam is directly congruent to the outgoing incandescent image, the optics which manage these signals must be multi-purpose and coupled between the constraints of each signal. Additionally, the outgoing signal is not a fixed path but rather a constantly changing path as the image is translated which adds to the necessity for tightly constrained parameters and corroborated simulation of the signal. Finally, as the purpose of this instrument is to be usable for a variety of samples, with hundreds of grid points, a robust automation/user protocol is required.

The purpose of this dissertation is to perform the next iteration of the design in regards to automation of the system and the implementation of a user interface. Chapter 2 describes a full systematic review of both the primary components included in Figure 1.3 as well as the opto-mechanics which couple these components. Some of these components were upgraded to improve repeatability. Chapter 3 describes the design and construction of a full-stack automation software which provides a user interface, automated back-end and database support for the device. Chapter 4 confirms the hyperspectroscopy function and demonstrates the functionality of the software. Chapter 5 includes a summary of the work completed in this dissertation, recommendations for future work and conclusions of the project.

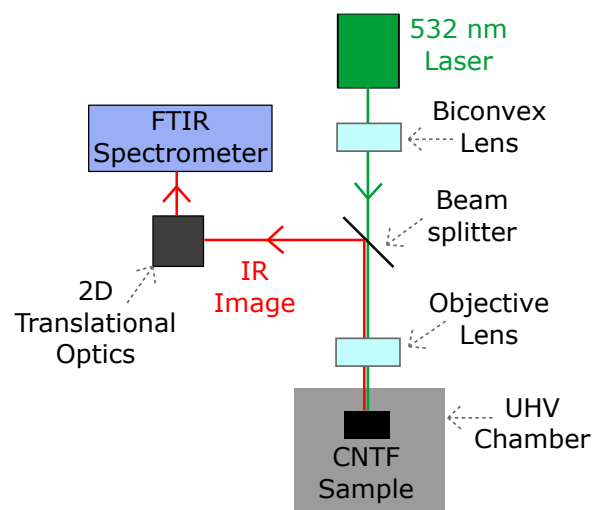


Figure 1.3: A block diagram of the primary components of the hyperspectrometer. The incoming signal is focused with a biconvex lens, passes through a beamsplitter, is focused by an objective lens and hits the sample in a Ultra-High Vacuum (UHV) chamber. The outgoing incandescent signal is magnified by the objective, is reflected by the beamsplitter, is moved using the translational optics and is scanned by the spectrometer.

Chapter 2

Opto-Mechanical System Design

2.1 Incident Optical Excitation Beam

This section describes the simulation and design of the optical system which directs and focuses a laser beam onto the sample.

2.1.1 Gaussian Beam Propagation

A Verdi V-5 solid-state diode-pumped frequency-doubled Nd:Vanadate laser from Coherent was used as the excitation source and had been mounted to the optical table prior to this study with an active cooling system as prescribed by the manufacturer [6]. The laser head is a hermetically sealed system of a vanadate gain medium, a lithium triborate (LBO) frequency doubling crystal, a single-frequency etalon, an optical diode, an astigmatic compensator and three cavity mirrors. A DC power supply unit provides power to the pumping diode and houses the CPU which controls the ramped heating of the LBO crystal to its operating temperature of 148°C as well as the diode, Vanadate and etalon temperatures via thermo-electric coolers. This system produces a laser beam with the specifications outlined in Table 2.1.

A series of mirrors were set up to guide the incoming beam from the location of the laser, around some unrelated equipment on the optical table, through a beam splitter responsible for splitting the incoming beam and outgoing signal, through an objective assembly responsible for focusing the beam onto the sample and finally

Table 2.1: Verdi V-5 Laser Output Specifications [6]

Parameter	Specification
Output Power	5W
Wavelength	532 nm
Beam Diameter	2.25 mm \pm 10%
Beam Full-Angle Divergence	<0.5 mrad
M^2	<1.1
Power Stability	\pm 1%
Noise	<0.02 rms
Polarization	<100:1, vertical, linear
Linewidth	<5 MHz rms
Pointing Stability	<2 μ rad/ $^{\circ}$ C

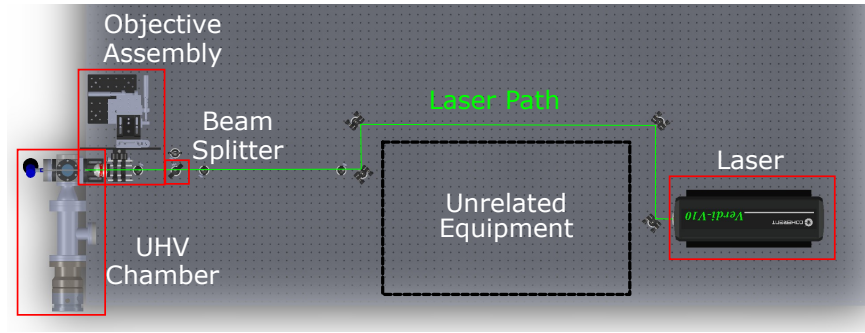


Figure 2.1: CAD rendering of the incident beam path from the laser, around unrelated equipment in its path, through the beam splitter, through the objective lens and onto the sample in the UHV chamber

to an UHV chamber which houses the CNTF sample. This system is shown in the Computer Aided Design (CAD) rendering in Figure 2.1.

Due to the low M^2 factor¹ of the laser beam, it can be assumed that the beam propagates with a Gaussian intensity profile [19]. A Gaussian ansatz is applied to the paraxial Helmholtz equation which governs a polarized time-harmonic electromagnetic beam, resulting in the paraxial Gaussian beam formula for a wave prop-

¹The M^2 value is a ratio between the beam parameter product (BPP) and the BPP of a Gaussian beam of the same wavelength. The beam parameter product is the ratio between the beam divergence angle and the beam waist [18]. M^2 represents the beam deviation from a Gaussian beam.

agating in the x direction. For a given waist radius ω_0 at a focus point, for a slowly varying function, the Gaussian beam formula results in Equation 2.1 where $\omega(x)$, $R(x)$, λ and $\eta(x)$ are the beam radius, radius of curvature, wavelength and Gouy phase of the wavefront respectively as a function of x as defined by Equation 2.2 to Equation 2.4 [11].

$$A(x, y) = \sqrt{\frac{\omega_0}{\omega(x)}} \exp\left(\frac{-y^2}{\omega(x)^2}\right) \exp\left(\frac{-iky^2}{2R(x) + i\eta(x)}\right) \quad (2.1)$$

$$\omega(x) = \omega_0 \sqrt{1 + \left(\frac{\lambda x}{\pi \omega_0^2}\right)^2} \quad (2.2)$$

$$R(x) = x \left[1 + \left(\frac{\pi \omega_0^2}{\lambda x}\right)^2\right] \quad (2.3)$$

$$\eta(x) = \frac{1}{2} \arctan \frac{\lambda x}{\pi \omega_0^2} \quad (2.4)$$

As shown in Figure 2.2, $x = 0$ is defined as the point where the wavefront is approximately planar resulting in $\frac{\lambda x}{\pi \omega_0^2} \ll 1$, $R(x) \approx \infty$ and $\omega(x) \approx \omega_0$. As x increases, the gaussian profile diverges such that $\frac{\lambda x}{\pi \omega_0^2} \gg 1$, $R(x) \approx x$ and $\omega(x) \approx \frac{\lambda x}{\pi \omega_0^2}$. The Rayleigh Range x_R is defined as the limit where $\frac{\lambda x}{\pi \omega_0^2} = 1$ as in Equation 2.5 [11]. The divergence angle θ is defined as the slope of the line defined by the Rayleigh Range as in Equation 2.6.

$$x_R = \frac{\pi \omega_0^2}{\lambda} \quad (2.5)$$

$$\theta = \frac{\lambda}{\pi \omega_0} \quad (2.6)$$

With the development of the laser diameter defined by the Gaussian beam formula, a Zemax Opticstudio [1] simulation was constructed to design the beam propagation through the optical system and ultimately the irradiation spot on the sample. The purpose of this simulation is to determine an optical configuration of the sample, viewport and objective lens such that the laser is focused to a spot diameter of approximately $100 \mu m$ on the sample surface (and to determine if ad-

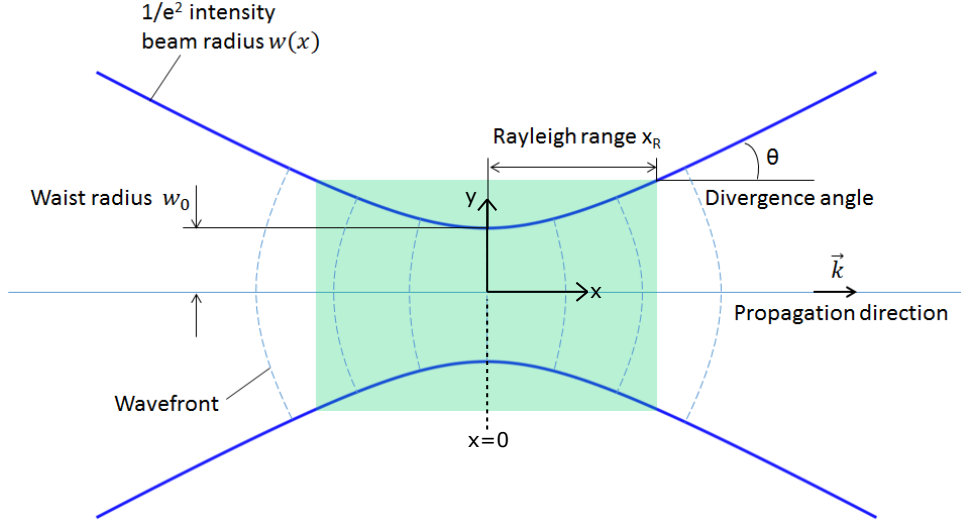


Figure 2.2: Schematic of Gaussian beam propagation [11]

ditional optics are necessary). The divergence angle θ and the output wavelength λ are defined by the manufacturer in Table 2.1 which results in a beam waist w_0 of 0.3387 mm as per Equation 2.6. Surface 1 was defined as the beam waist and Surface 2 was defined as the laser output port as shown in Figure 2.3. The wavelength was set to 532 nm as defined by Table 2.1.

A Gaussian Beam Paraxial Divergence merit function was applied which sets the beam waist at Surface 1 to 0.3387 mm, and optimizes the thickness of Surface 1 (distance from the beam waist to the laser output) to achieve a beam radius of 1.125 mm at Surface 2 as defined in Table 2.1. The merit function resulted in the beam waist being located 2035.548 mm behind the laser output port as shown in ???. In reality, the beam of course does not extend behind the laser, but in the case of the simulation this virtual surface dictates the Gaussian development of the beam throughout the entire system.

2.1.2 Beam Focusing via Objective Lens

The Thorlabs LMM-25X-P01 infinity corrected objective lens, which was used to focus the beam onto the sample employs a set of two internal mirrors to focus a beam incoming from infinity to the focal point at a Working Distance (WD) of

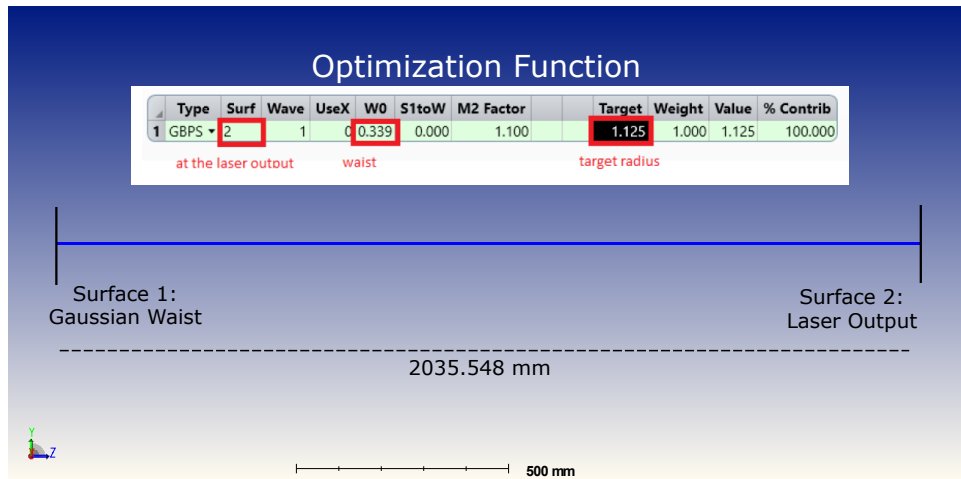


Figure 2.3: Beam waist defined as Surface 1, distance from the waist to the laser output port is optimized to have a beam diameter of 2.25 mm as described by the manufacturer. This results in a distance of 2035.548 mm.

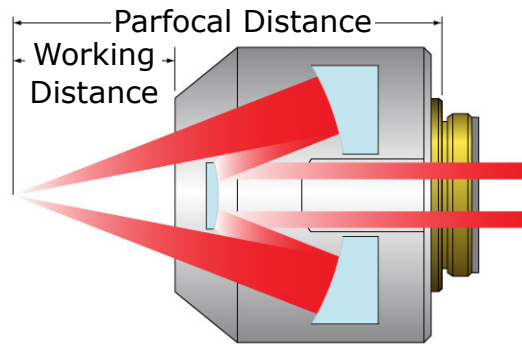


Figure 2.4: Schematic of beam tracing through objective lens from right to left [12]

12.5 mm away from the outer surface of the objective lens as in the schematic in Figure 2.4. The objective lens was mounted to a micro-adjustable assembly which allowed it to be manipulated on the micron scale in the x,y and z planes as in the CAD rendering in Figure 2.5.

The Zemax lens file for the objective lens was loaded into the Gaussian beam simulation defined in Section 2.1.1. A 3.8 mm thick Kurt J. Lesker VPZL-275UZ

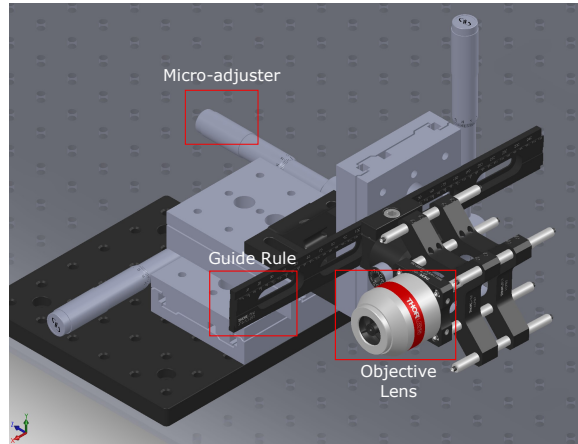


Figure 2.5: CAD rendering of objective lens assembly

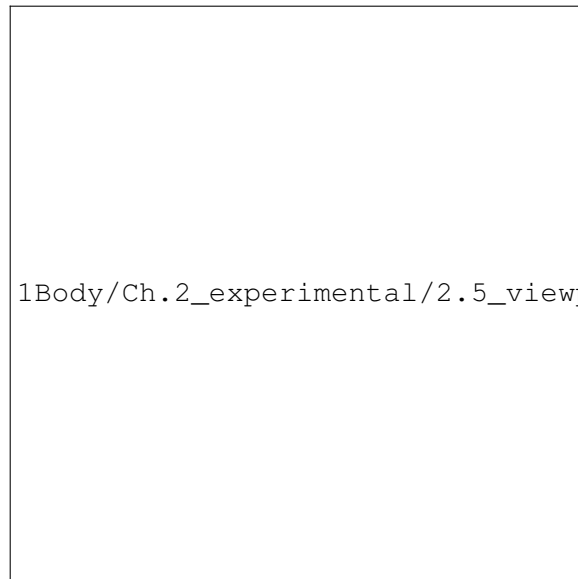


Figure 2.6: CAD rendering of UHV view-port in line with objective lens

Zinc Selenide (ZnSe) view-port [20] was placed 20 mm away from the objective lens output port as per the UHV CAD schematic in Figure 2.6. The image plane was defined within the vacuum chamber as 3 mm from the surface of the view-port. The real part of the ZnSe index of refraction is defined within Zemax by a range of wavelength values applied to a fitting regime which has been experimentally defined at room temperature. The imaginary component of the index of refraction is assumed to be zero for all dielectric materials in Zemax Opticstudio (a setting which cannot be changed). In the case of ZnSe, the wavelength range is defined as $0.55 \mu\text{m}$ to $18 \mu\text{m}$ applied to a Sellmeier 1 Formula at 20°C as in Equation 2.7 [21] where n is the index of refraction and $K_1 = 4.298$, $K_2 = 6.278e - 1$, $K_3 = 2.895$, $L_1 = 3.689e - 2$, $L_2 = 1.435e - 1$, $L_3 = 2.2085e3$ are the Sellmeier coefficients [1]. As this wavelength range does not include the laser wavelength of 532 nm, the material file was copied for ZnSe and the lower limit of the wavelength range was reduced to 500 nm (applying the same Sellmeier coefficients). This approximation will need to be validated through further experimentation on the transmission characteristics of the ZnSe window for the wavelengths in question.

$$n^2 - 1 = \frac{K_1 \lambda^2}{\lambda^2 - L_1} + \frac{K_2 \lambda^2}{\lambda^2 - L_2} + \frac{K_3 \lambda^2}{\lambda^2 - L_3} \quad (2.7)$$

If the incoming beam is of a sufficient diameter (approximately 4 mm), then the objective lens will function as intended with the beams focusing at the WD of 12.5 mm as in Figure 2.7. The incoming 2.25 mm laser beam does not have the required beam diameter to produce the necessary divergence to refract past both mirrors as in Figure 2.8, leading to a 99.2519 % insertion loss.

Further optical elements were designed to change the path of the beam in such a way that it will create a $100 \mu\text{m}$ spot on the sample when directed through the objective lens as described in Section 2.1.3.

2.1.3 Spot Size Control and Optimization

A bi-convex lens was chosen which would simultaneously direct the beam off-axis through the objective in such a way that it reaches the sample surface, while focusing its diameter such that a $100 \mu\text{m}$ spot size is achieved. This lens would also provide a method to control the incoming spot size while maintaining the objective

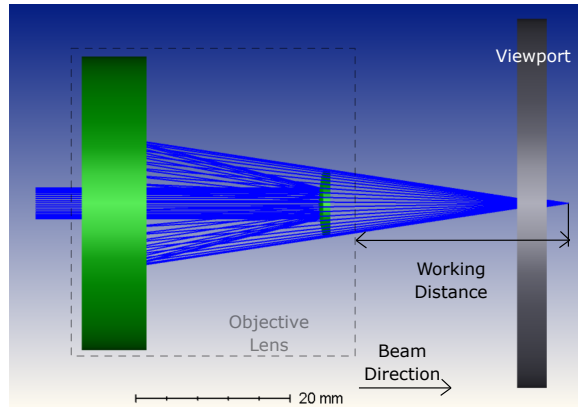


Figure 2.7: Zemax rendering of objective lens ray tracing from left to right with an incoming beam diameter of 4 mm. With this diameter, the beam would reach the sample surface after passing through the viewport.

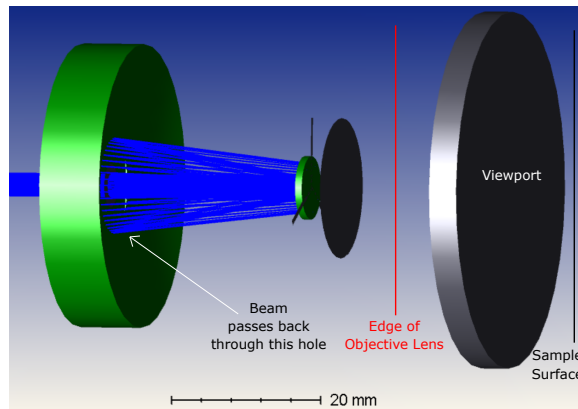


Figure 2.8: Zemax rendering of objective lens ray tracing from left to right with an incoming beam diameter of 2.25 mm. The beam is refracted by the second mirror back through the hole in the first mirror which it emerged from, rather than being refracted by said mirror back towards the sample.

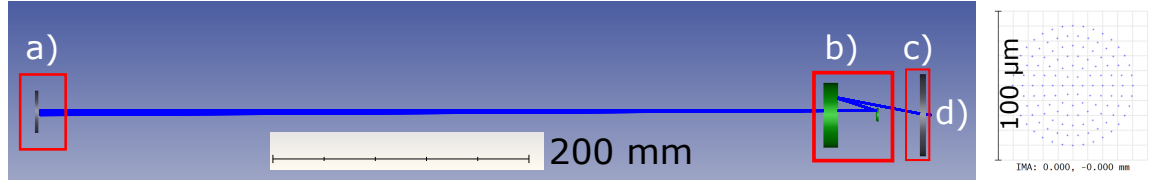


Figure 2.9: Zemax rendering of bi-convex lens implementation. Laser beam is incoming from the left to a) the bi-convex lens, through b) the objective lens, through c) the viewport and finally to d) the beam terminating at the sample surface. The resulting spot rendering is shown on the right.

lens position for the outgoing signal. As opposed to a single optical element to expand the beam to an acceptable diameter, this method would provide decoupling of spot size control and the objective lens position. This lens was placed into the simulation at approximately 50 cm behind the objective lens assembly which places it out of the way of the other optical elements on the table. A coordinate shift of 2.121 mm in the y direction (perpendicular to the direction of the laser beam) was set on the surface before the bi-convex lens and a reciprocal coordinate shift of -2.121 mm was set on the surface following the bi-convex lens. This shift in the simulation path represents shifting the lens off axis to direct the focused beam off the objective lens axis.

The distance of the sample to the view-port surface, the bi-convex lens parameters (thickness, radius of curvature) and the exact placement of the bi-convex lens was fed through a series of Gaussian Beam Paraxial Divergence merit function optimization iterations with the objective of producing a 100 μm diameter spot on the surface of the sample. The resulting optimized bi-convex lens was found to be a Thorlabs 1" diameter LB1869 N-BK7 glass biconvex lens with a focal length of 500 mm [22] placed at approximately 450 mm behind the objective lens, with the sample placed 3 mm behind the view-port. The resulting Zemax simulation demonstrates the function of the bi-convex lens to direct the beam through the objective lens to a spot size of 100 μm on the sample surface as shown in Figure 2.9.

An Allied Vision Technical Guppy Pro F-125 type 1/3 C-mount CCD camera mounted to a Navitar 6000 zoom system was used to provide in-situ imaging of the sample surface through the view-port [7][8]. The zoom system was comprised of a

Table 2.2: CCD Camera + Zoom System Specifications [7][8]

Specification	Value
Nominal WD	175 mm
Fine Focus Range	12 mm
Numerical Aperture (NA)	0.011 to 0.035
Magnification	1.16X to 7.4X
Field of View (FOV)	5.2 mm to 0.81 mm
Resolve Limit	30.3 μm to 9.52 μm
Depth of Field (DOF)	4.13 mm to 0.41 mm

C-mount couple to the CCD camera, a 3.3X zoom short adapter tube, a 12mm fine focus 6.5X prime zoom lens and a 0.5X lens attachment. This assembly provides the specifications outlined in Table 2.2.

The camera was mounted to two micro-adjustment stages and set on the table at the nominal WD of 175 mm away from the view-port as depicted in Figure 2.10. The micro-adjustment stages (as well as the 12mm fine focus) allow the camera position to be finely tuned to a particular focal image plane on the sample. The interior of the UHV chamber was illuminated from the top view-port, and an image was taken from the camera focusing on a CNT sample inside the chamber as in Figure 2.11.

The bi-convex lens was set on the optical table at approximately 500 mm behind the entrance port of the objective lens at an off-axis shift of approximately 2 mm as shown in Figure 2.12. A 532 nm 5 mW laser pointer [23] was used to align the mirrors, biconvex lens and objective lens to focus on the sample surface within the UHV chamber. The laser spot size can be controlled by adjusting the axial position of the bi-convex lens as demonstrated in Figure 2.13.

2.2 Ultra-High Vacuum Chamber Design

An UHV system was designed by previous colleagues to house and position the CNTF samples and to provide a modular mounting point for accessories in the future. As shown in Figure 2.14, the vacuum mechanics include an a) Agilent Technologies TwisTorr 84 FS Turbo Pump [24], b) a connection to an Agilent

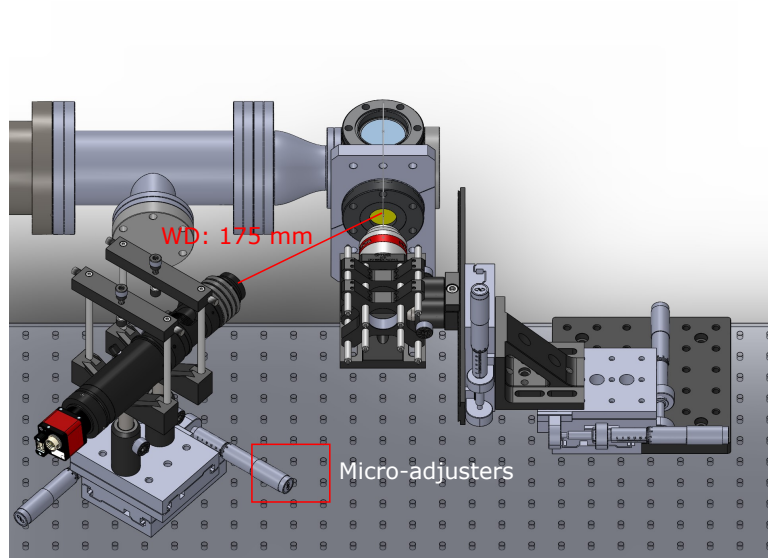


Figure 2.10: CAD schematic of optical setup for in-situ imaging camera. The camera is mounted on micro-adjusters for fine positional adjustment and placed at the working distance of the camera to begin the focusing process.

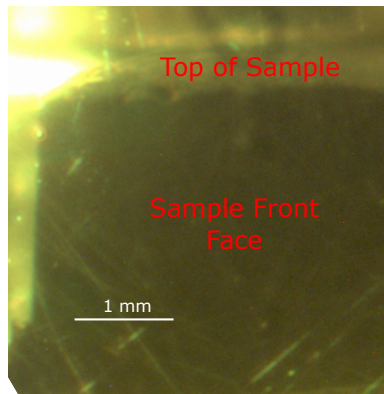


Figure 2.11: Image collected by focusing the in-situ camera on the sample surface

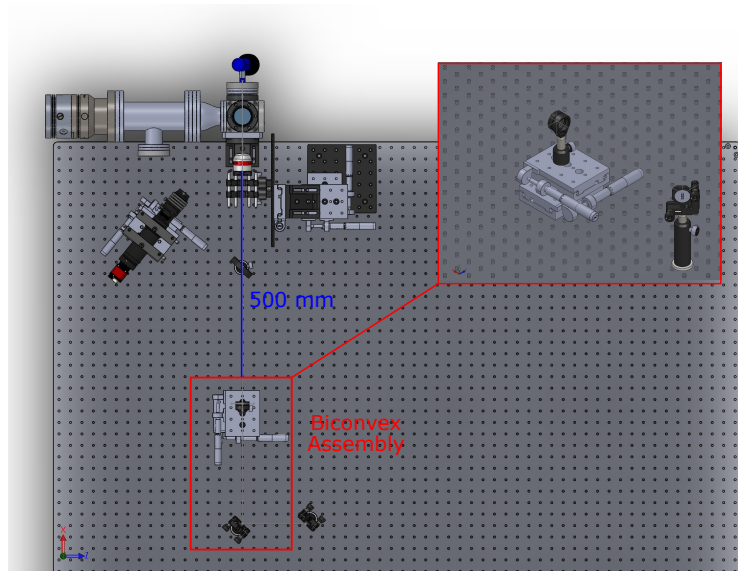


Figure 2.12: CAD rendering of biconvex lens setup on optical table. The lens is initially placed at 500mm from the objective lens as per the simulations, and finely adjusted using the micro-adjuster stages.

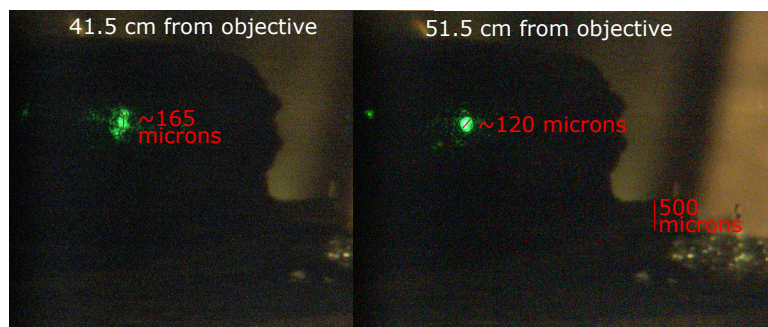


Figure 2.13: Spot size adjustment via axial shifting of biconvex lens with approximately 53% laser power reaching the sample

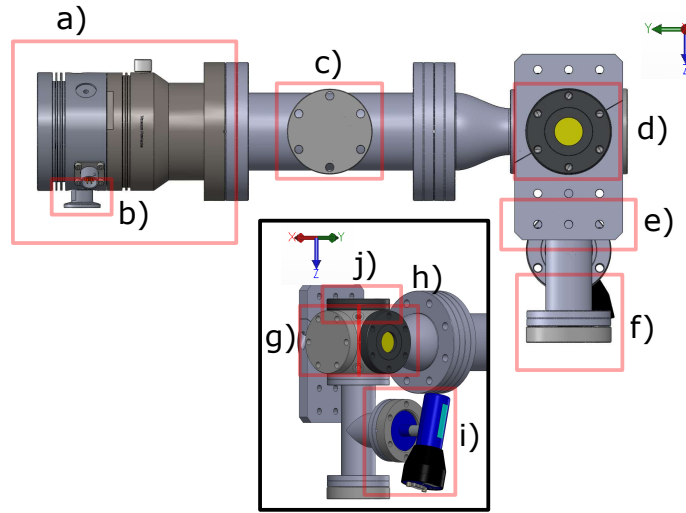


Figure 2.14: CAD schematic of UHV chamber including a) a turbo pump b) a connection to dry scroll pump c) a blank flange d) a ZnSe viewport e) a mounting plate f) a connection point for a cold cathode gauge g) a future electronics access point h) a rear viewport i) a pirani gauge j) a top viewport

Technologies SH-110 Dry Scroll Vacuum Pump (only connector shown), f) a connection point for a KJL943 Cold Cathode Vacuum Sensor [25] and i) a KJL275804 Convection Enhanced Pirani Gauge [26]. The scroll pump/pirani gauge and turbo pump/cold cathode gauge are used to pump the system pressure down to approximately 0.2 Torr and UHV respectively.

The center cube houses the sample stage and is fastened to the optical table via a Kimball Physics mounting bracket shown in e). The flange shown in d) is the ZnSe viewport described in Section 2.1.2 which transmits the incoming optical signal and outgoing infrared signal. Flanges g), h) and c) provide mounting points for peripheral devices such as electrical feed through points, additional viewports or other vacuum components. The flange shown in j) is currently fitted with a Kodial Glass viewport to visualize the sample in situ.

Figure 2.15 depicts a sample stage and mounting fixture which were designed

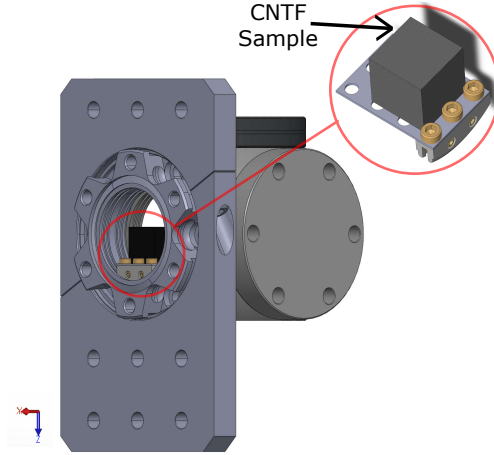


Figure 2.15: CAD schematic of sample stage and mounting device for CNTF

and built out of Kimball Physics eV Parts [27]. The mounting fixture was mounted directly to the vacuum flange.

2.3 Design of Hyperspectroscopy Opto-Mechanics

2.3.1 Simulation of Infrared Signal Collection and Propagation

As depicted in Figure 2.16, the infrared signal of interest which is produced by the CNTF hot spot passes through the same ZnSe viewport described in Section 2.1.2 and is focused onto an image by the objective lens (a). This image is reflected off of the beamsplitter (b), a set of periscope mirrors (c), the motorized linear stage mounted mirrors which perform the translation necessary for hyperspectroscopy (d) before entering the port of the FTIR spectrometer described in Section 2.3.4 (e).

In order to collect spatially resolved hyperspectra, the image produced by the hot spot must be focused at the entrance port of the FTIR spectrometer. A Zemax Opticstudio simulation of the outgoing signal path was constructed by first defining a field at the object plane with a height of $100\text{ }\mu\text{m}$ to represent the hot spot. Two wavelengths were defined at $2\text{ }\mu\text{m}$ and $10\text{ }\mu\text{m}$ to cover a broad IR spectral range. The elements from the objective lens were reversed with respect to the order defined in Section 2.1.3, and the ZnSe viewport was placed at the same distance from

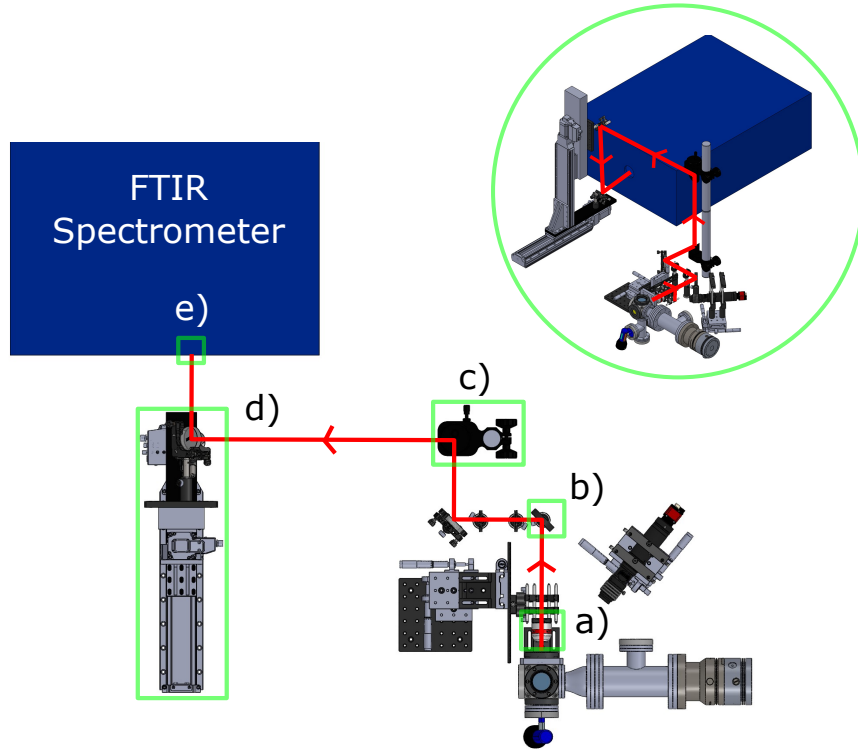


Figure 2.16: CAD rendering of the outgoing image path a) through the objective lens b) reflected by the beamsplitter c) reflected upwards by the parascopic mirrors d) reflected through the translational optics e) collected by the spectrometer. The inset image depicts the beam path through the parascopic mirrors and the translational optics.

the objective lens as defined in Section 2.1.3. The distance from the objective lens to the spectrometer entrance port was set at 2 m which is the approximate distance due to the table layout. If the incandescent spot was placed at the position of the laser spot in Section 2.1.3 as is expected from prior CNTF hot spot experiments [10], the principal rays would be blocked by the objective as shown in Figure 2.17. This means that if the objective lens were to be configured as described in Section 2.1.3, the IR image of interest would not travel past the objective lens, meaning the position of the objective lens must be altered. As both the incoming and

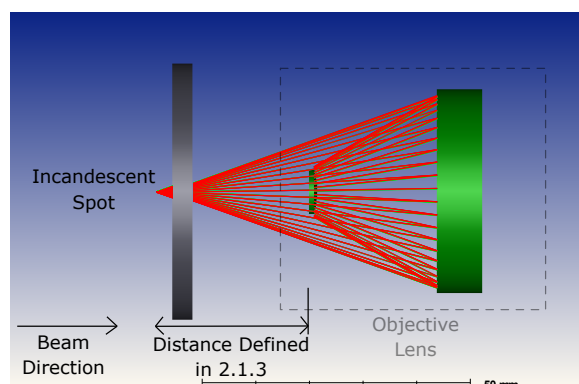


Figure 2.17: Zemax ray tracing demonstrating ray block at objective lens when objective is configured as defined by Section 2.1.3

outgoing signals depend on the objective positioning, both simulations had to be optimized in parallel.

A series of optimization functions were performed between the two sets of parameters until a local minimum was achieved. These parameters include the positioning of the biconvex lens, the position of the objective lens, and the distance to the spectrometer entrance port. As shown in Figure 2.18, while maintaining an incoming laser spot of $100\ \mu\text{m}$ the optimal positioning of the objective lens is 19.658 mm away from the viewport with a path of 2025 mm from the output of the objective lens to the FTIR entrance port. This results in a magnification of $\sim 156\times$, which would produce a 15.6 mm diameter inverted focused image at the entrance port of the FTIR from a $100\ \mu\text{m}$ image. Figure 2.18 depicts the incoming and outgoing beam path with the objective lens positioned as described above (a,c), confirmation of the correct laser spot size (b), and confirmation of a focused image at the entrance port of the spectrometer (d). All optimal parameters are included in Table 2.3.

Using this optimized positioning as a starting point, the image side depth of focus and object side depth of focus were explored using the standard test image in Zemax Opticstudio. Figure Figure 2.19 demonstrates that the image plane depth of focus is much larger ($\sim 30\text{cm}$) than the object plane depth of focus ($\sim 10\ \mu\text{m}$) for an IR wavelength range of $2\ \mu\text{m}$ to $10\ \mu\text{m}$. Practically, this means that the image formed at the FTIR entrance port is much more sensitive to the objective

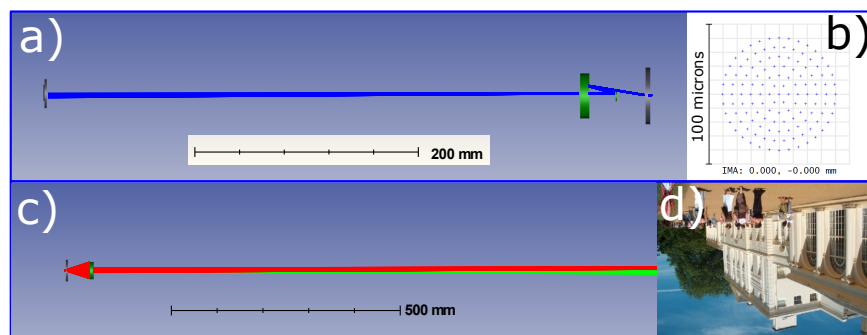


Figure 2.18: Corroborating zemax simulations for the incoming signal (a), a 100 µm laser spot (b), the outgoing signal (c) and a focused image at the FTIR entrance port (d). The image used is the default test image found in Zemax Opticstudio.

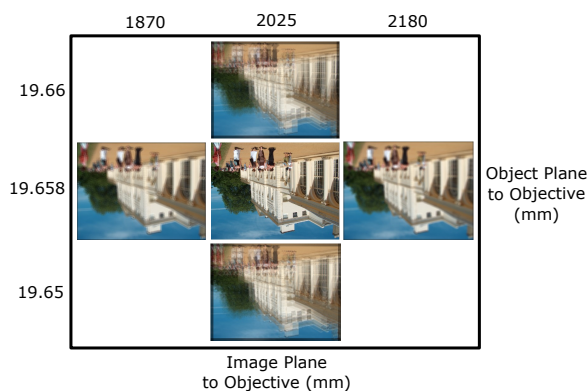


Figure 2.19: Demonstration of depth of focus with regards to the objective lens and spectrometer positioning. Changing the position of the objective lens will have a much larger impact on the image focus than changing the distance from the object to the spectrometer

lens positioning than the positioning of the outgoing optics. It should also be noted that the image will be inverted by the objective in this configuration.

2.3.2 Global Calibration Source Alignment

To test the alignment of the optics and confirm the predicted image formation, a silicon carbide (known as “Globar”, Coorstek Model 301 Ceramic Igniter) broadband

Table 2.3: Optimized Optical Setup Parameters

Specification	Value
Sample to viewport	3 mm
Viewport to objective	19.658 mm
Objective to spectrometer	2025 mm
Magnification	156x
Laser spot diameter	100 μm
IR image spot diameter	15.6 mm

infrared source [28] was placed inside the vacuum chamber. This is used as a calibration source because its IR emission spectrum is known to be very close to that of a blackbody radiator as in Figure 2.20. Additionally, the Globar source emits a strong visible signal which can be used to visualize the image as it propagates through the optical system. As the Globar source heats to $\sim 1500^\circ$ in its nominal voltage range [28], the viewport was removed to ensure it was not damaged. A Xantrex LXQ30-2 DC power supply was used to apply 13.2 V across the globar source as its temperature is known to be 1580°C at that voltage [28]. As shown in Figure 2.21, a 100 μm precision pinhole aperture was placed in an X/Y translation mount which was mounted to the UHV chamber in place of the viewport. This configuration would create a representative “hot spot” at the surface of the aperture as the Globar would emit a relatively uniform IR/visible signal throughout the chamber, and some of that signal would emit through the pinhole aperture.

To align the optics to the IR signal a laser pointer was used to create a visual alignment scheme. As shown in Figure 2.22, the first step in the alignment process is to send a visible laser pointer through the beam splitter and the objective and to align it with the aperture. As the beam splitter has some degree of reflection at the 532 nm wavelength of the laser pointer, it will reflect a perpendicular beam to the right where two apertures are placed in line as shown in Figure 2.22 a). Then the laser pointer is placed behind these two apertures and used to align the rest of the optical system. As the IR signal will reflect perpendicularly off of the beam splitter the same as the laser in step a), the laser in step b) will be in line with the IR signal and can be used to visually align the signal. As shown in Figure 2.23, this spot

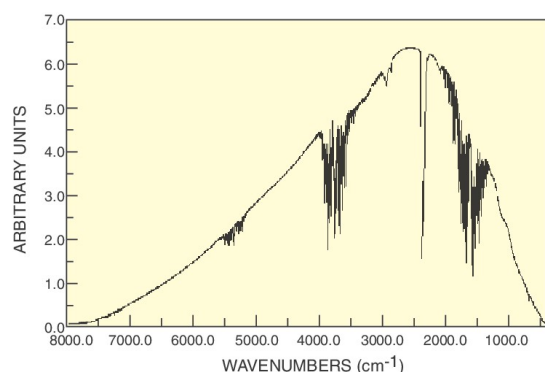


Figure 2.20: Emission spectrum of Globar IR source

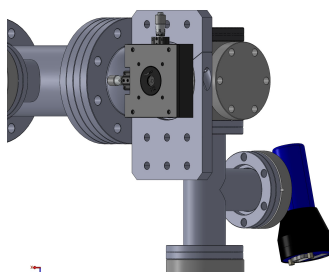


Figure 2.21: CAD rendering of 100 μm aperture mounted to vacuum chamber

alignment can be confirmed with the visible camera described in Section 2.1.3.

An ElectroPhysics MicronViewer 7290A IR camera was placed at the same distance from the objective as the FTIR entrance port and a rotating mirror was placed to direct the signal to the IR camera rather than the FTIR as in Figure 2.24. If the image can be confirmed as focused on the IR camera, then it would follow that the spot is also focused at the entrance port when the rotating mirror is switched between the two paths. A 1100 nm long-pass filter was fixed to the camera to ensure that its detector is not damaged by the visible range of the Globar signal.

Once this alignment was performed, no signal was detected on the camera or the spectrometer due to insufficient signal power. An alternative method was

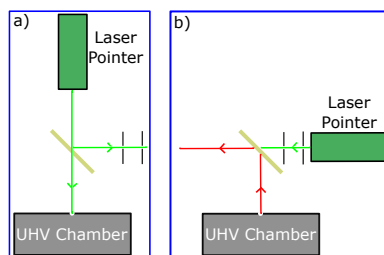


Figure 2.22: Schematic showing alignment two step procedure where a laser (green line) is aligned to the hot spot and alignment apertures are placed on the table (a) which are then used to align the optics with the infrared signal (red line) (b)

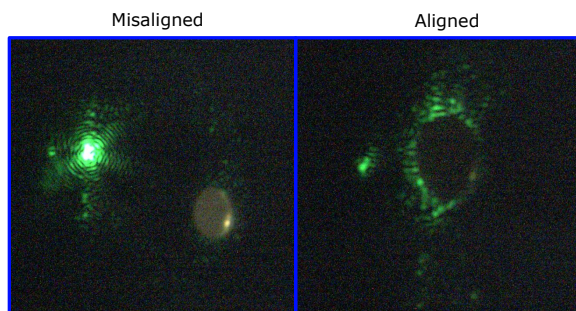


Figure 2.23: Alignment procedure with laser pointer and 100 μm illuminated aperture

pursued in Section 2.3.3 which would provide a strong enough signal to confirm that the IR image was being received by the spectrometer.

2.3.3 Visible Source Alignment

First the Globar element was placed inside a parabolic mirror to try and direct more signal towards the pinhole aperture, which still resulted in insufficient signal power. Then the Globar was replaced with a 3200 K colour temperature high intensity fiber light source [29] behind the same pinhole aperture. This source would provide a strong enough visible signal to confirm the image at the entrance port of the spectrometer, and was tested to prove that the signal could be picked up by the IR camera.

The visible image was confirmed at the entrance port of the spectrometer with

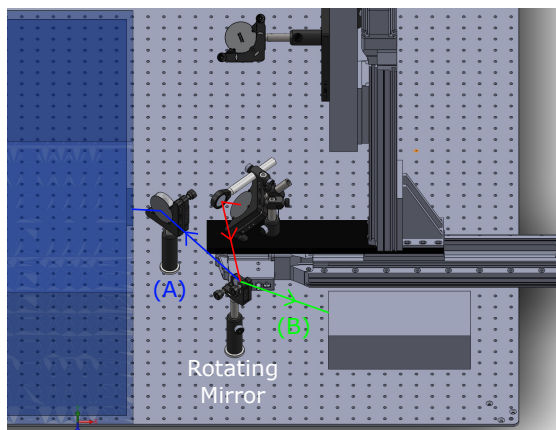


Figure 2.24: CAD rendering of IR camera alignment. If distance A equals distance B, then a focused image at the IR camera would be focused at the spectrometer entrance port once the rotating mirror is shifted between path A and B.

the expected magnification. The IR image was also confirmed with the IR camera confirming that there is an IR image being received at the spectrometer. Unfortunately this signal provided insufficient power to be detected by the spectrometer.

To increase the image power, as shown in Figure 2.25 the fiber light source was removed from the chamber, the 1/4" fiber bundle was fitted with a 2.5 cm diameter steel tube to direct the signal towards the mirrors and placed directly next to the motorized stage mounted mirrors. This would greatly increase the power density as there would be no magnification from the objective and no power loss from the rest of the intermediate mirrors. A 1100 nm long-pass filter was placed in front of the spectrometer to ensure the detector was not damaged and an aperture of 3mm was placed over the port to provide spatial resolution. The spectrometer is designed to receive a focused image as described in Section 2.3.4 and shown in the optical diagram in Figure 2.26. The image size was limited by the size of the mirrors, creating an image with a radius of a few cm. A signal was confirmed on the spectrometer by blocking/passing the signal to the entrance port and observing a significant change in the FTIR real-time spectra collection. The motorized stages were moved in each direction by a specified amount, and the corresponding im-

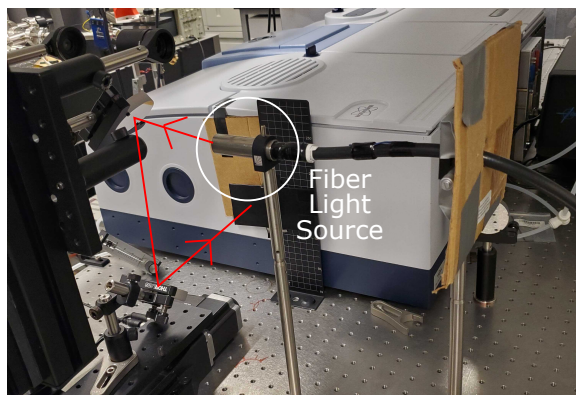


Figure 2.25: Fiber light source mounted directly in front of the motorized mirrors fitted with steel tube to increase signal power

age translation of that same amount was confirmed on both the IR camera and the spectrometer entrance port proving the hyperspectroscopy method was functional.

2.3.4 Fourier Transform Infrared Spectroscopy Spectra Collection

A Bruker VERTEX 70 FTIR spectrometer was used to collect the infrared spectral data from the image described in Section 2.3.3. The beam path enters the exterior port from the right through a KBr window, is fed through a Michelson interferometer and processed by a detector which produces a characteristic spectrum via Fourier transform. This beam path within the FTIR spectrometer is shown in Figure 2.26.

The Michelson interferometer is composed of a broadband KBr beamsplitter, a scanning mirror and a stationary mirror as shown in the schematic in Figure 2.26. At the onset of the measurement the emission source is split by the beamsplitter (in an ideal case 50 percent transmission and 50 percent reflection) into two beams which reflect off the moving and stationary mirrors respectively. At this point the mirrors are equidistant from the beamsplitter, which results in a maximum signal amplitude as the beams recombine perfectly in phase and reflect towards the detector. As the movable mirror scans to/from the beamsplitter through a preset range, the relative amplitude of the resulting signal creates a cosine wave. The interfering waves will be completely in phase whenever the path difference between the two

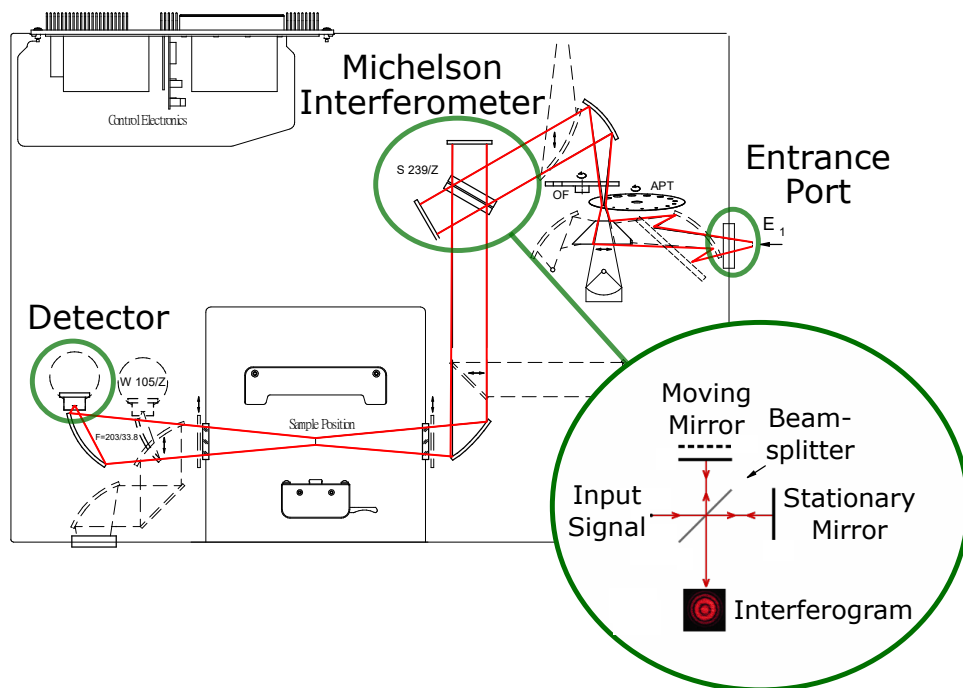


Figure 2.26: Beam path within FTIR spectrometer with emission entering through the exterior entrance port and interferometer schematic

waves is an integer multiple of the wavelength. Inversely, the signal will be completely out of phase (a minimum intensity) when the distance is an integer multiple of half the wavelength. This relationship provides a correlation between the movable mirror position and the wavelength of radiation entering the interferometer. The plot of this relationship is called an interferogram.

For a broadband source, the intensity of all wavelengths is completely in phase at zero path difference creating a maximum intensity at this point. As the mirror moves, the range of signals in the band become increasingly out of phase resulting in a complex oscillatory signal with decreasing amplitude. The signal is decomposed into its spectral components (individual sinusoidal functions) in the time domain and fed through a fast Fourier transform in order to produce a spectrum in the frequency domain. A background scan is subtracted from the emission spectrum to produce an IR spectrum representing the thermal emission entering the spectrometer.

Chapter 3

Automation Software Design

3.1 Program Initialization

A full-stack software called “HypIR” was built to facilitate automated measurements including a front-end written in Python via the Tkinter open source GUI, a back-end written in C/Python to manage the communication between the spectrometer and the linear stages and an SQL database accessed via SQLite3 to manage and record all experimental parameters. This network is represented by the block diagram shown in Figure 3.1 which shows each script/component of the software, the area of software it belongs to, and the communication protocols used to connect these codes together. The code scripts are not included due to their confidential nature.

The program is executed via the OPUS FTIR software by selecting File, External Program, navigating to the C:/HypIR/Final drive and selecting the control.exe program as shown in Figure 3.2. This executable file is the centralized control code which is written in C and compiled in Visual Studio. IT should be noted that this software was built using the current 2021 Win32 API. Any windows operating system updates that include changes to this environment may require a patch. After execution, the script first establishes a communication channel to the spectrometer via the Named Pipe client/server protocol which is included in the Win32 API [30]. If this connection is unsuccessful, an error function “cerror” will be tripped which writes a standard error to the Win32 API and terminates the program. A text docu-

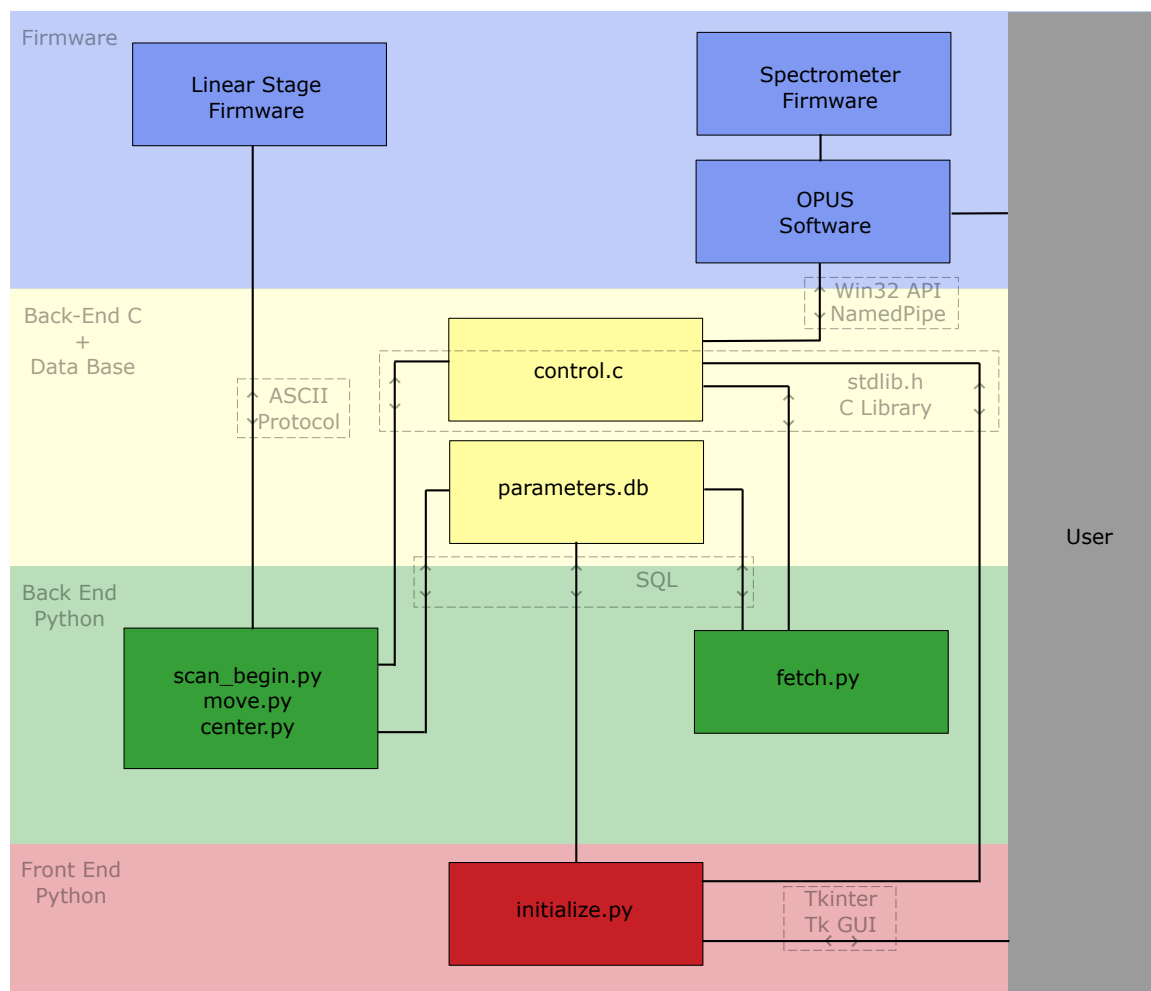


Figure 3.1: Block diagram representation of full-stack HypIR software including communication channel protocols

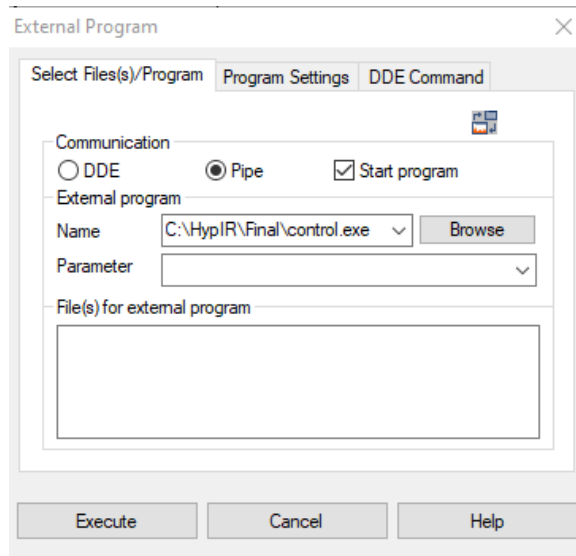


Figure 3.2: Select the control.exe executable through the OPUS External Program function

ment is included in the script directory (c:/HypIR/test_out.v1.txt) which is used to capture information at key points in the process should an error arise which is not accounted for.

Once a connection is successfully established, the control.exe executes the initialize.py program with the condition to wait until initialize.py completes before proceeding.

3.2 Opening Page

The initialize.py script contains the majority of the user interface, parameter management and experimental setup. As shown in Figure 3.3 the opening window includes a field to insert the users name, the date and any notes about the measurement, a button to begin the run sequence, a button to open the stage manual control and a button to alter the initial optical setup parameters. The values in the three entry fields are committed to the database (parameters.db) when the “Run” button is pressed. If any fields are left blank, the value is set as “BLANK” when the new line is committed to the database.

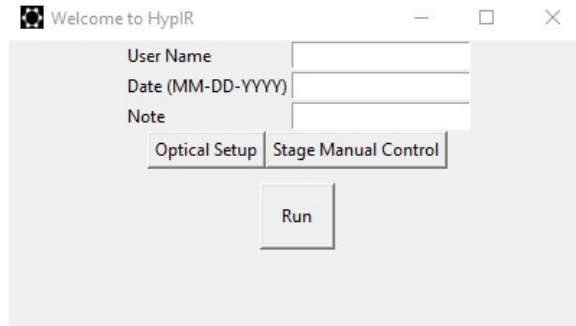


Figure 3.3: Welcome page of HypIR software

3.3 Linear Stage Control Page

When the “Stage Manual Control” button is pressed, the window shown in Figure 3.4 appears. This page can be used to move the image into position using the linear stages manually, and to update the positioning/state of the stages. It should be noted that the program allows the user to input limits for the horizontal stage to ensure that the stage does not run into optics during the automated scanning procedure. This function is not built into the manual stage control as during this study the optical system was constantly changed between runs, making this limit invalid. The user should always be watching the system when using the manual control to avoid impact. Section 3.2 includes the user input to update the horizontal stage limit for automation purposes.

There are 4 buttons which move the x/y stages by 1 mm in each direction respectively and 4 buttons that move them by 5 mm respectively. Each time one of the buttons is pressed, the serial port is checked, the parking state of the stages is checked, the correct stage is selected and moved an absolute distance by the prescribed amount. If there becomes an issue with the connection to the stages, then an error window will arise as in Figure 3.5.

In the bottom left corner there are two buttons which check the serial connection, check the parking state, park/unpark the stages respectively, and change the label from “Parked” to “Unparked” respectively. All stages must be parked before the computer is restarted, or they will require calibration which could misalign the system. The “Set Center” button finds both stages current positioning and sets that

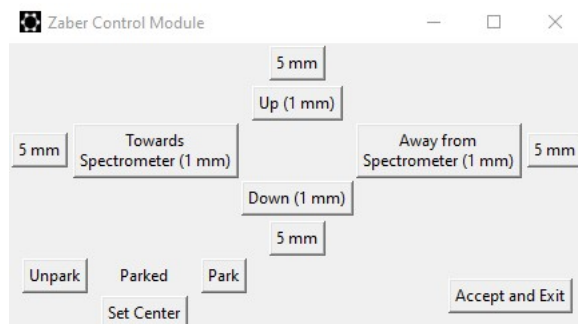


Figure 3.4: Stage control page

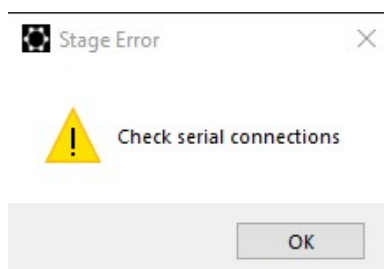


Figure 3.5: Stage error message

as the center position which is committed to the database. This parameter is helpful as multiple experiments can be executed from precisely the same starting position. The “Accept and Exit” button checks the connection, reads the parking state of the stages, parks both stages and closes the stage control module.

3.4 Optical Setup Page

Once the “Optical Setup” button is pressed, the optical setup window appears as shown in Figure 3.6. First the software sets the current position as the center position, and updates X Stage Center and Y Stage Center. The xpm file path, image magnification and x-stage spatial limit are read from the database and listed. Once the user presses “Update” the labels will update if there are new values in the entry fields and all values will be committed to the database. If the “Select FTIR XMP File” button is selected, it opens the folder where XPM files are held and the user can select a file which will update the label and commit to the database.

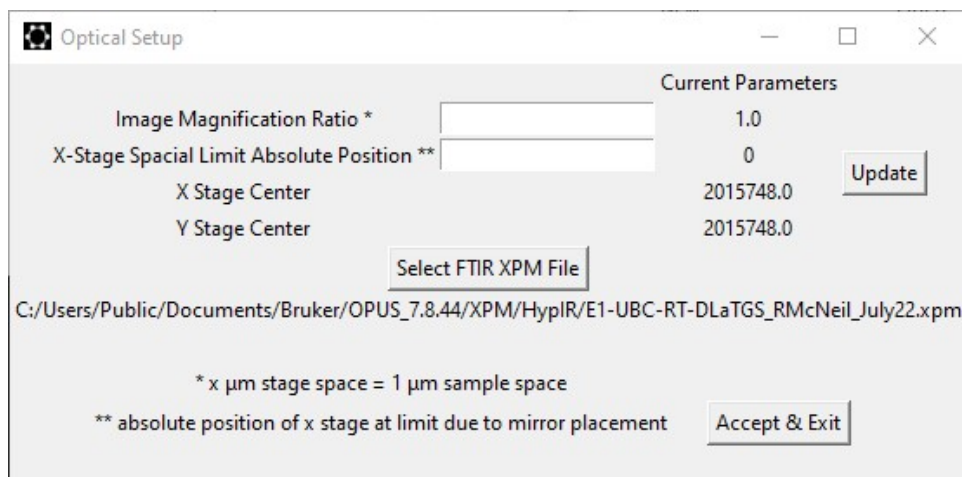


Figure 3.6: Optical setup input page

The image magnification ratio describes the scaling between the image space and the object space. This is used to convert the movement increments across the sample which the user will input to the increments the stages will have to move. The x-stage spatial limit can be updated if there are additional optics in between the spectrometer and the x-stage which the stage could run into. If it is set to 0, then there is no limit to the x-stage movement within the full stage range, as was the case for all the measurements taken in this study. The XPM file can be created in the OPUS software and contains all the spectrometer measurement parameters that will be fed to the hyperspectroscopy experiment. The “Accept & Exit” button will close this window.

3.5 Parameter Window

Once the “Run” button is pressed, the parameter window appears as shown in Figure 3.7. The X scan length/Y scan length and X number of steps/Y number of steps describe the size of the scan across the sample in both directions and the number of scan points in each direction accordingly. Once the “Update” button is pressed, first the steps are checked because they must be odd values based on how the movement sequence is coded. If the steps input as even numbers, the Y scan length interferes with the X stage spatial limitations or one of the fields is left

Current Parameters	
X scan length (µm)	50000.0
Y scan length (µm)	50000.0
Number of X Steps (odd)	5
Number of Y Steps (odd)	5
Resulting X Step Size (µm):	10000.0
Resulting Y Step Size (µm):	10000.0

Figure 3.7: Scan parameter input page

Figure 3.8: Error messages

blank, an error message is thrown as shown in Figure 3.8.

If the “Run With Background” button is pressed, then the variable “home” will be recorded as 1, recording that a background scan is necessary. The program then confirms with the user that the source is blocked/off for a background scan as in Figure 3.9. If this query is declined the program will revert to the home page. The program then retrieves the experimental parameters from the database and moves the stages to the starting position for the scan as shown in Figure 3.10. At this point the initialize.py program is terminated and the control.exe program will proceed.

If the “Run Without Background” button is pressed, then the variable “home” will be recorded as 0, recording that a background scan is not necessary. The program then confirms with the user that the source is on for a hyperspectroscopy scan as in Figure 3.11. If this query is declined the program will revert to the home

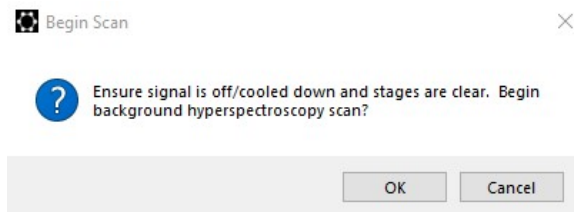


Figure 3.9: Check with user for background scan

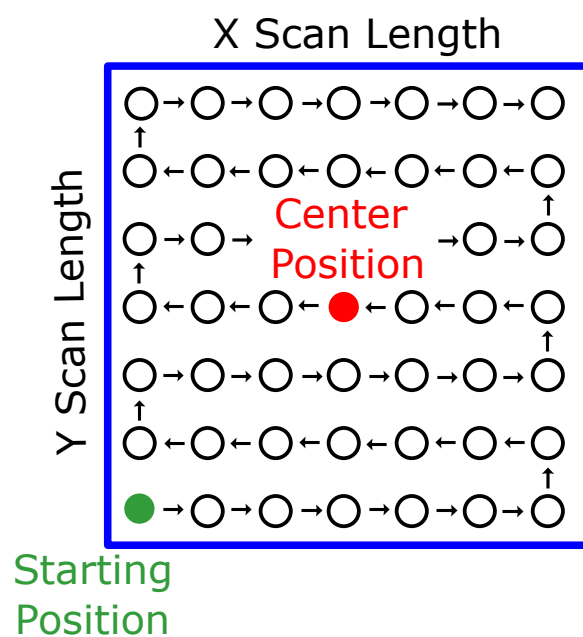


Figure 3.10: Scan procedure schematic

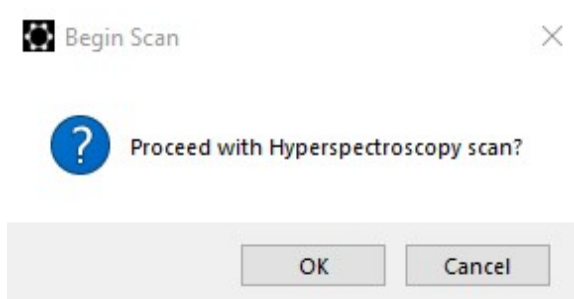


Figure 3.11: Check with user for sample scan

page. The program then retrieves the experimental parameters from the database and moves the stages to the starting position for the scan as shown in Figure 3.10. At this point the initialize.py program is terminated and the control.exe program will proceed.

3.6 Data Retrieval

When the initialize.py program completes, the control.exe program will execute fetch.py which retrieves and parses all the applicable experimental parameters from the database. Control.exe checks to see if home is set to 1 or 0, indicating the need for a background run. The program constructs the three different system calls to move the stages one step up (image moves right), down (image moves left) and away from the spectrometer (image moves down) respectively. If the scan begins at the bottom left corner, then these movements would scan the image in the path described by Figure 3.10.

3.7 Scan Execution

If a background sequence is necessary, the program executes a loop which performs the scan/move operation as per the schematic in Figure 3.10. The spectrometer scan is performed using a “run” function which communicates with the spectrometer for the scan and saves each scan in the grid in the folder which is defined by the XPM file. Each subsequent movement step is performed by running one of the three move.py calls described above. Once the full hyperspectra is collected, center.py is called which re-centers the image for the sample scan.

Once the image is centered, the program performs the “ascii” function which executes a macro “OPUS_TO_ASCII_BY_FOLDER.MTX” [31]. This macro will ask the user for an origin/destination folder for the spectra files. The macro then takes each file in the origin folder, transforms it from a proprietary file type to a csv file and saves it in the destination folder. The user can ensure proper file organization at this point so that background files are not confused with sample files.

At this point, the program will execute start_scan.py which will first ask the user if the source is on and ready for a hyperspectroscopy scan as in Figure 3.11.

If this query is declined the program terminates. If it is accepted, then the program will move the stages to the bottom left starting position, and perform the exact same loop as in the background scan, including the file processing macro. Finally the program performs center.py again to leave the system at the center position, and terminates.

If home = 0 and a background scan is not necessary, the program performs the loop as above, executes the file processing macro, executes center.py and terminates.

Chapter 4

Results and Discussion

To demonstrate the function of the control software from Chapter 3, the spectrometer and the optical system, a series of representative scans were performed using the high intensity light source described in Chapter 2 as the sample source.

4.1 Scan Procedure

To begin a hyperspectroscopy scan, the user should first use the IR camera to confirm the optical alignment. The user can then clear the spectrometer entrance port and use the real time spectra collection in the OPUS software to visually establish the background scan as shown in Figure 4.1. The FTIR entrance port can then be opened to the signal (with the long-pass filter in place to avoid detector damage), and the change in IR signal can be visually confirmed using the same real time spectra capture as shown in Figure 4.2. If a signal is not detected, or the signal is weak, alignment can be adjusted in the HypIR software as described in Section 3.3. Once HypIR has been booted, the user can input their user details, change any optical setup parameters and reset the center position as described in Chapter 3. It should be noted that the user must close all windows in OPUS (such as the real time spectra capture) before running any scans as these will cause the program to stall due to the spectrometer firmware limitations.

For the following scans a resolution of 20 cm^{-1} was chosen with 50 scans per measurement, scanning across the entire range limited by the spectrometer optics

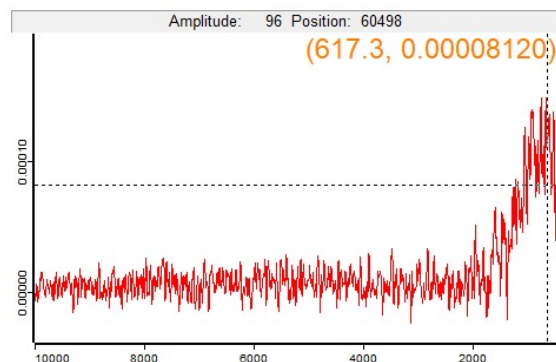


Figure 4.1: Background real time spectra capture in OPUS software

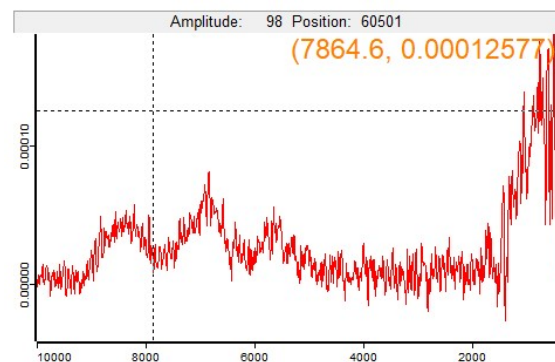


Figure 4.2: IR signal confirmed with real time spectra capture

which is $10,000\text{ cm}^{-1}$ to 380 cm^{-1} . This resolution and scan count is sufficient for scanning the representative image described in Section 2.3.3 as the signal should be relatively uniform and the purpose of these scans is not to discern minute details. The scan resolution, scan count and hyperspectroscopy parameters can be tuned according to the sample of interest. Once the scan is complete, the resulting background files and sample files should be stored in separate directories which do not hold any other files.

4.2 Device Calibration

In order to extract the temperature map from the collected hyperspectra, a calibration must be performed to account for the effects of the spectrometer response. The following describes the process which is performed by a MATLAB code which is unavailable due to confidentiality. This code is an altered version of one written by previous colleagues [31].

The internal Near Infrared (NIR) tungsten lamp source is used as a reference to calibrate the hyperspectra to the detector response and spectrometer optics. As this source is a quasi-blackbody thermal emitter [32], covers the approximate wavelength range the fiber light source is emitting (approx 9000 cm^{-1} to 4000 cm^{-1}) and would include the effect of the internal spectrometer optics, this was chosen as an effective calibration source.

To produce this calibration file, first a background scan was produced with the emission entrance port covered so as to block any external IR radiation. Then the NIR source was selected, and a scan with the same spectral parameters as the subsequent sample scans (resolution, scan range, scan count etc.) was performed. This would produce a curve which represents the emission from the quasi-black body source attenuated by the spectrometer optics and detector response.

The background spectrum is subtracted from NIR spectra creating the reference curve, and the peak is located. This peak wavenumber is fed into Wein's displacement law as in Equation 4.2 which is derived from Planck's Law in units of energy radiance as a function of wavenumber as in Equation 4.1 [33] which gives the approximated temperature of the NIR. The constants in both formulas are the speed of light c , Boltzmann's constant k , Planck's constant h and a unitless constant $a_3 = 2.82143937212$. Using this temperature a theoretical Planck curve can be constructed using Equation 4.2. The theoretical Planck curve and the reference curve are normalized, the reference curve is divided by the theoretical curve and the final curve is normalized to produce the calibration file. As the Planckian behaviour assumed of the NIR source has been removed from the spectrum, the resulting data represents the attenuation from the spectrometer optics and the detector response.

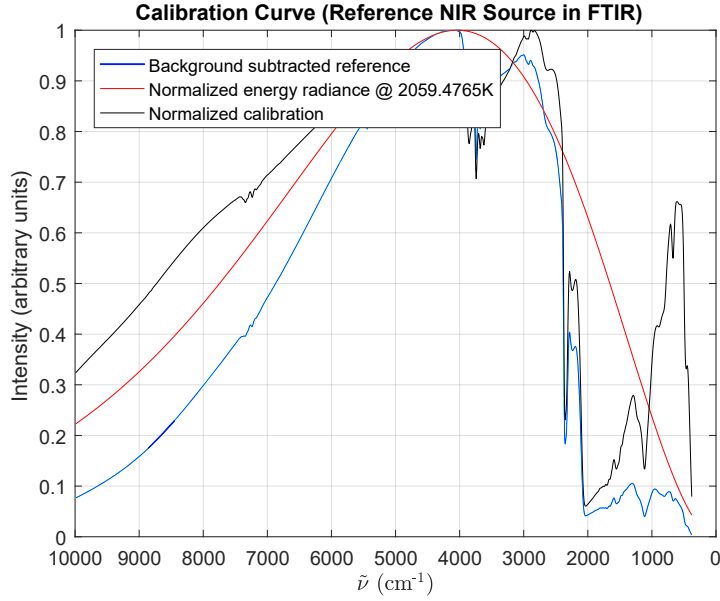


Figure 4.3: Normalized NIR reference spectrum (blue), Normalized energy radiance at 2059.4765 K (red), Normalized final calibration curve (black)

$$L(\tilde{\nu}) = 2hc^2\tilde{\nu}^3 \frac{1}{e^{\frac{hc\tilde{\nu}}{kT}} - 1} \quad (4.1)$$

$$\tilde{\nu}_{peak} = \frac{a_3 kT}{hc} \quad (4.2)$$

The results from the steps above are demonstrated in Figure 4.3. The calculated temperature based on Wein's displacement law is 2059.48 K. The actual temperature of the NIR source is unknown and it is possible this approximation is incorrect.

4.3 Temperature Extraction

After the measurement is complete, the background hyperspectra are subtracted from the sample hyperspectra. Then the post processing code loops through each spectrum to perform the following data cleaning steps: subtract the background

spectrum at that grid point, divide by the calibration curve and normalize, linearly interpolate over the CO₂ absorption band (2400 cm^{-1} to 2800 cm^{-1}), smooth the data, trim off the data outside the device spectral bounds and trim out negative data. At this point the spectrum at that grid point is stored in a larger matrix and the curve-fitting can proceed. The spectrum is fit to the Planck function included in Equation 4.1 with 2 fitting coefficients a and b representing Equation 4.3 and Equation 4.4 respectively via the non linear least squares regression method. MATLAB automatically calculates a range of goodness of fit metrics which are stored along with the coefficients. The temperature at each point is then extracted using Equation 4.4, and 2D maps of the temperature and corresponding R² values are constructed.

$$a = 2hc^2 \quad (4.3)$$

$$b = \frac{hc}{kT} \quad (4.4)$$

4.4 Results

A series of representative measurements were taken using the high intensity fiber light source to demonstrate the effectiveness of the software, and the hyperspectroscopy functionality.

A few coarse scans (7×7) over $10\text{ cm} \times 10\text{ cm}$ were taken initially in order to locate and center the hot spot signal. These hyperspectra were then processed through the post processing code, and the fit quality could be checked. As shown in Figure 4.4, the data do not fit Planck's law closely, but do scale with the intensity of the signal which is proportional to the location on the spot.

As shown in Figure 4.5, low resolutions can be used to identify the location of the spot, while the higher resolution can be used to gather finer detail on the temperature maps. It takes approximately 45 seconds per scan at the scan resolution as stated in Section 4.1, and the scan time scales linearly with the number of grid points. So a 5×5 scan would take about 20 minutes, a 7×7 scan would take about 40 minutes and an 11×11 scan (the resolution used for the remainder of the

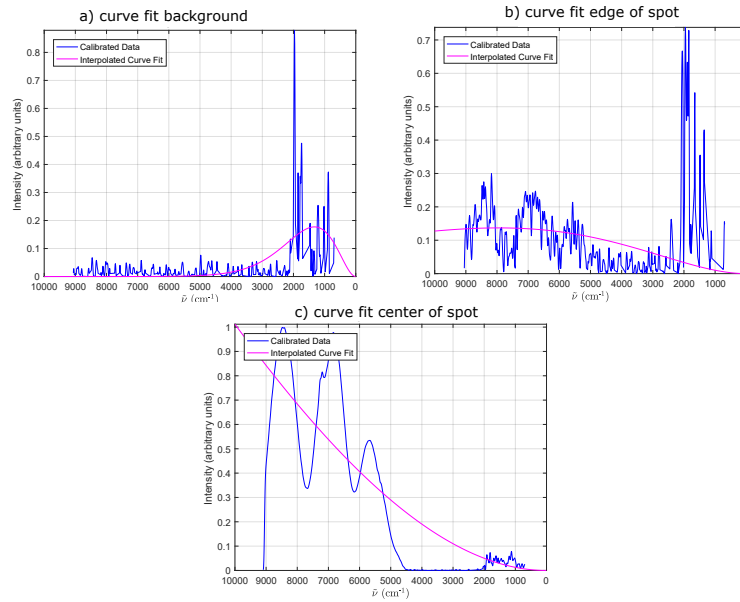


Figure 4.4: Poor curve fitting, but proportional intensity to spot location

document unless stated otherwise) would take about 95 minutes. These times will double when a background scan is performed.

As expected, the fiber light source did not emit quasi-blackbody radiation as a CNTF would be expected to as shown in Figure 4.4, which meant the quantitative temperature results would not be physically meaningful. However, as shown in Figure 4.6, when the light source was switched between approximately half and full power, the hot spot temperature scaled accordingly demonstrating the spectrometer response to a change in the incoming signal power.

To demonstrate that translation in the stage movements will correspond to an equal translation in the IR image, a scan was first taken with the spot approximately placed at the center as shown in Figure 4.7 b). Then 2 scans were completed with the x stage moved 2 cm forwards and backwards. As shown in Figure 4.7 a) and c), this moves the image by 20mm in each direction respectively, confirming the hyperspectroscopy function.

There is some significant distortion seen Figure 4.7 c), which is due to the fact that the image is comprised of the component of the IR radiation emitted from

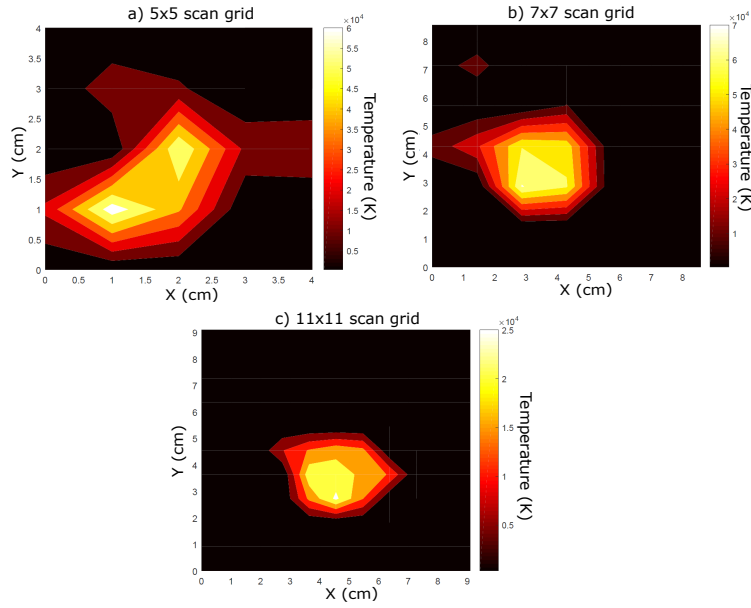


Figure 4.5: Increasing resolution from a)5x5 b)7x7 c)11x11

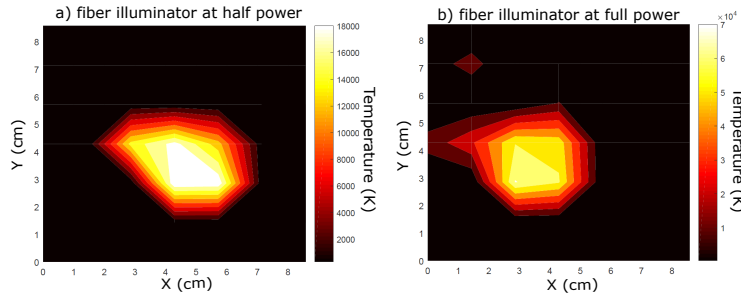


Figure 4.6: Change in IR signal when source was switched between a) half power and b) full power

the fiber light source which happens to be aligned to the mirrors directed at the spectrometer. Essentially this means that the object being imaged is the area of the translating mirrors rather than a focused image (smaller than the mirrors) in the case of a CNTF hot spot source. If the stages are aligned such that the spot is generally in the center of the scan, than it would follow that the greatest percentage of rays coming from the light source which are directed perpendicular to the optical axis will be incident on the detector, creating a resolved hot spot.

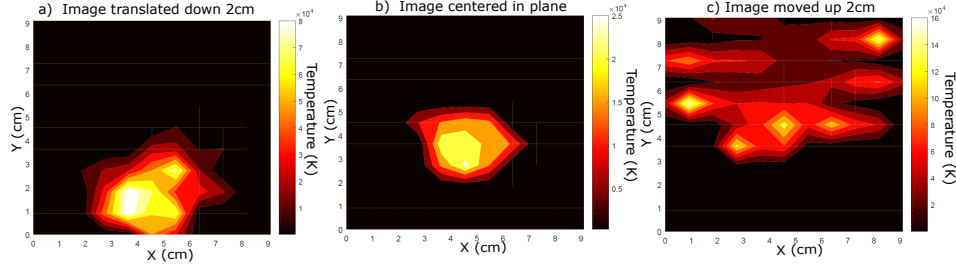


Figure 4.7: Approximately 2 cm translation of image a)down and c)up corresponding to 2 cm stage translation. Distortion in figure c) corresponds to signal dispersion due to lack of image focus

As the mirrors deviate from this center, the detector will be picking up the signal coming from the edges of the mirrors which means it will be picking up the much more dispersed edge of the signal, creating this distortion. Additionally, the fiber light source emission may deviate by an unknown amount to the optical axis of the system, which would distort the image depending on the location of the mirrors.

As demonstrated by the curve fitting in Figure 4.4, the spectral profile of the light source is far from a black body source. There seems to be a broad peak which is attenuated by two absorption bands which results in the 3-peak spectrum. As the halogen lamp source emission spectrum is known to be continuous and well fitted to Planck radiation [34], this 3-peak behaviour is most likely due to either unknown optical components inside the lamp housing or the fiber bundle at its output. This results in poor fitting to Planck's Law, which follows that the temperature value which is calculated from that curve may not be representative. Although the temperature magnitudes may not be representative, the center hot spot with a continuous gradient to room temperature as seen in Figure 4.5 and Figure 4.6 are consistent with a centralized source. This profile as well as the confirmed translation and change in temperature with power as in Figure 4.6 and Figure 4.7 indicate that the hyperspectra are representative of the source signal.

4.5 Material Parameter Extraction

To extract a map of thermal conductivity and emissivity from these temperature maps, a finite element analytical model in 1 dimension was developed which deploys an energy balance equation to the optically induced hot spot. This model and the subsequent python code are unavailable due to confidentiality. The model was tested and implemented successfully, but as it was not applicable to the enclosed results due to its assumption of optical heating, it was not included in this dissertation. This model and code can be expanded to 2 dimensions in the future.

Chapter 5

Conclusions and Future Work

5.1 Summary and Conclusions

The goal of this dissertation was to demonstrate and apply a systematic engineering design approach to the Hyperspectroscopy system which had been built to proof-of-concept by previous group members. The structure and progress of this study is laid out in the schematic in Figure 5.1. The work of previous colleagues which preceded this study included the discovery of the heat trap effect (Chapter 1) and the construction of a device to study that effect which included a laser, incident optical system, UHV chamber, sample stage, outgoing optical system, translational optics and FTIR spectrometer.

A systematic engineering review was performed which began by learning and demonstrating the functionality of each component which had already been built, and its subsequent application to the objectives of the system were reviewed (Chapter 1 and Chapter 2). To understand the ultimate physical limitations of each component within the device, a complete theoretical review was performed which included all associated Gaussian optics, geometric optics, Planck's law, interferometry, full-stack programming and finite element modelling. To transform the theory into actionable objectives and constraints, all processes were recreated with simulations. The optics were modelled in Zemax Opticstudio, the mechanics were modelled in Solidworks and a software architecture was built to support each subsystem. In terms of the physical system, a few upgrades were achieved such as a

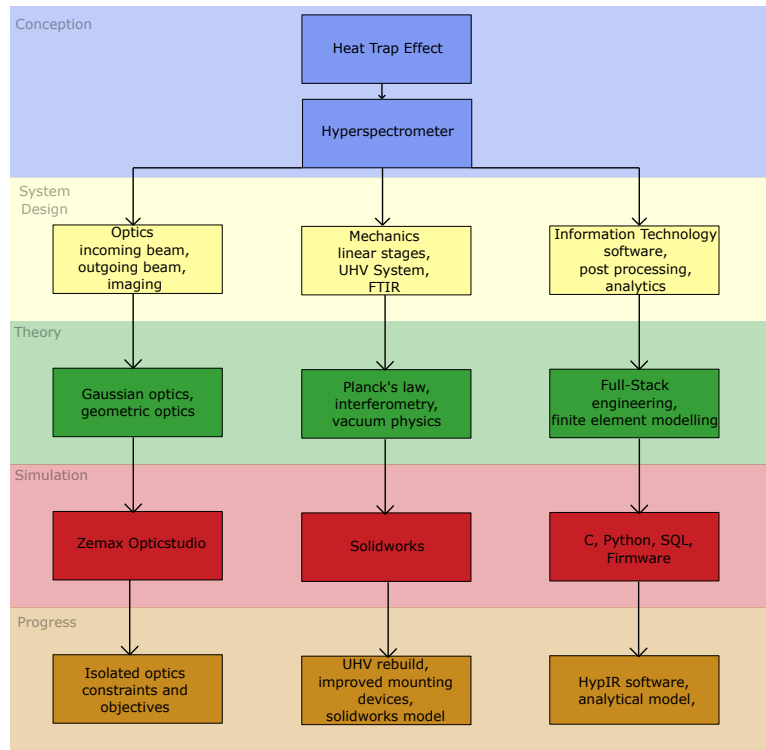


Figure 5.1: Flow schematic for design process and project progress

adjustment of the UHV system, a redesign of some mounting devices to improve experimental reproducibility and an improvement in the in situ imaging optics. Software and data processing design were selected as the primary design goal as it would provide more generalized user accessibility, and facilitate experimental variation as the design evolved.

A full-stack automation software was constructed which includes a user interface front-end, a device control back-end and database support for parameters. The software effectively performs some common error handling, transforms user input to control output, communicates effectively with the spectrometer and motor components and performs the hyperspectroscopy scan.

This study was successful in identifying a critical engineering step to moving the design forward which was a robust software component. This study was also successful in performing an initial mapping via simulations of the ultimate

constraints which will dictate future design, as well as exposing the instabilities and impractical components in the system. The rigorous engineering approach applied in this study to the instrument in its early stages of development is critical to maximizing its future potential. This study provides the groundwork on which a successful product can be built, and the framework to maintain forward progress towards a reproducible product.

5.2 Future Work

The software built during this study is a fully functioning prototype, but some improvements can be made to advance the software towards a commercial product. In terms of the complete software architecture, if the entire program could be coded in Python (rather than communicating with the spectrometer in C), this would allow for a collective executable which would make the program more transferable. This could be achieved by translating the client/server connection protocol provided by Bruker (written in C) to Python.

The error handling of the program is functional for current possible errors, but should be updated to be able to process unknown errors as well. A longer term goal would also be to communicate with the spectrometer manufacturer in order to bypass the OPUS software entirely which is currently the only method to connect an external program to the spectrometer. The user interface was primarily built for function, which means ease of use and aesthetic design could be improved in the future.

In terms of opto-mechanics, once the optics are aligned to the current setup with a CNTF sample, unwanted degrees of freedom should be removed from each optical device. This could mean mounting the biconvex lens described in Section 2.1.3 to a linear stage such that its off-axis coordinate shift is fixed as per the Zemax Opticstudio simulations completed in this study, with allowable movement towards/away from the objective lens to provide spot size control. This same concept could be applied to other optical components such as the periscopic mirrors, translational mirrors and beamsplitter, where angles and distances which do not provide function to the device are fixed with precision mounting equipment.

Bibliography

- [1] “Opticstudio.” [Online]. Available: <https://www.zemax.com/products/opticstudio>
- [2] “Solidworks.” [Online]. Available: <https://www.solidworks.com/>
- [3] F. Lundh, “An introduction to tkinter,” *URL: www.pythonware.com/library/tkinter/introduction/index.htm*, 1999.
- [4] “Sqlite3.” [Online]. Available: <https://www.sqlite.org/index.html>
- [5] H. D. E. Fan, G. A. Sawatzky, J. F. Young, and A. Nojeh, “Hyperspectroscopy: A tool for high-spatial-resolution temperature mapping of electron emitters,” in *2017 30th International Vacuum Nanoelectronics Conference (IVNC)*, 2017, pp. 44–45.
- [6] “Verdi v series.” [Online]. Available: <https://www.coherent.com/lasers/laser/verdi-v-series>
- [7] “Zoom 6000® lens system.” [Online]. Available: https://navitar.com/products/imaging-optics/high-magnification-imaging/zoom-6000/?creative=487313072570&keyword=&matchtype=b&network=g&device=c&gclid=CjwKCAiAl4WABhAJEiwATUnEF01IKF-ywAhPLM7EGigyQUZwEHLvRP_mtOHv_ohSTs9YotRq068IJRoCyN4QAvD_BwE
- [8] “Allied vision guppy pro f-125 1/3” ccd monochrome camera.” [Online]. Available: <https://www.edmundoptics.com/p/allied-vision-guppy-pro-f-125-13-ccd-monochrome-camera/23183/>
- [9] I. Dumé, “Scientists delve deeper into carbon nanotubes,” *Physics World*, vol. Transport Properties, 2013. [Online]. Available: <https://physicsworld.com/a/scientists-delve-deeper-into-carbon-nanotubes/>

- [10] M. Chang, H. Fan, M. Chowdhury, G. Sawatzky, and A. Nojeh, "Heat localization through reduced dimensionality," *Physical Review B*, vol. 98, 10 2018.
- [11] "Understanding the paraxial gaussian beam formula." [Online]. Available: <https://www.comsol.com/blogs/understanding-the-paraxial-gaussian-beam-formula/>
- [12] "Reflective microscope objectives." [Online]. Available: https://www.thorlabs.com/newgrouppage9.cfm?objectgroup_id=6933&pn=LMM-15X-P01
- [13] L.-M. Peng, Z. Zhang, and S. Wang, "Carbon nanotube electronics: recent advances," *Materials Today*, vol. 17, no. 9, pp. 433–442, 2014. [Online]. Available: <https://www.sciencedirect.com/science/article/pii/S1369702114002582>
- [14] K. Mizuno, J. Ishii, H. Kishida, Y. Hayamizu, S. Yasuda, D. N. Futaba, M. Yumura, and K. Hata, "A black body absorber from vertically aligned single-walled carbon nanotubes," *Proceedings of the National Academy of Sciences*, vol. 106, no. 15, pp. 6044–6047, 2009. [Online]. Available: <https://www.pnas.org/content/106/15/6044>
- [15] P. Yaghoobi, M. V. Moghaddam, and A. Nojeh, "'heat trap': Light-induced localized heating and thermionic electron emission from carbon nanotube arrays," *Solid State Communications*, vol. 151, no. 17, pp. 1105–1108, 2011. [Online]. Available: <https://www.sciencedirect.com/science/article/pii/S0038109811002602>
- [16] M. Vahdani Moghaddam, P. Yaghoobi, G. A. Sawatzky, and A. Nojeh, "Photon-impenetrable, electron-permeable: The carbon nanotube forest as a medium for multiphoton thermal-photoemission," *ACS Nano*, vol. 9, no. 4, pp. 4064–4069, 2015, pMID: 25769341. [Online]. Available: <https://doi.org/10.1021/acs.nano.5b00115>
- [17] P. Yaghoobi, M. Vahdani Moghaddam, and A. Nojeh, "Solar electron source and thermionic solar cell," *AIP Advances*, vol. 2, no. 4, p. 042139, 2012. [Online]. Available: <https://doi.org/10.1063/1.4766942>
- [18] "Lasers and laser-related equipment — Test methods for laser beam widths, divergence angles and beam propagation ratios," International Organization for Standardization, Standard, 2021.

- [19] H. Kogelnik, "Chapter 6 - propagation of laser beams," ser. Applied Optics and Optical Engineering, R. R. SHANNON and J. C. WYANT, Eds. Elsevier, 1979, vol. 7, pp. 155 – 190. [Online]. Available: <http://www.sciencedirect.com/science/article/pii/B978012408607450013X>
- [20] "Vpzl-275uz." [Online]. Available: <https://www.lesker.com/viewports/viewports-cf-flanged-exotic-lens/part/vpzl-275uz>
- [21] D. B. Leviton, B. J. Frey, and T. Kvamme, "High accuracy, absolute, cryogenic, refractive index measurements of infrared lens materials for JWST NIRCcam using CHARMS," in *Cryogenic Optical Systems and Instruments XI*, J. B. Heaney and L. G. Burriesci, Eds., vol. 5904, International Society for Optics and Photonics. SPIE, 2005, pp. 222 – 233. [Online]. Available: <https://doi.org/10.1117/12.619306>
- [22] "Lb1596 - n-bk7 bi-convex lens, Ø1", f = 60.0 mm, uncoated." [Online]. Available: <https://www.thorlabs.com/thorproduct.cfm?partnumber=LB1596>
- [23] "Galileo 532 nm green laser pointer." [Online]. Available: <https://www.laserglow.com/product/galileo-green-laser-pointer>
- [24] "Twistorr 84 fs turbo pump." [Online]. Available: <https://www.agilent.com/en/product/vacuum-technologies/turbo-pumps-controllers/turbo-pumps/twistorr-84-fs-turbo-pump>
- [25] "Series 943." [Online]. Available: <https://www.lesker.com/newweb/gauges/pdf/943kjl.pdf>
- [26] "Kjl275804." [Online]. Available: <https://www.lesker.com/gauges/convection-kjlc-2/part/kjl275804>
- [27] "ev parts." [Online]. Available: <https://www.kimballphysics.com/shop/ev-parts>
- [28] "Globar." [Online]. Available: <https://www.coorstek.com/english/industries/consumer-household/household-durables/igniters/igniter-specs/>
- [29] "Osl1 - high intensity fiber light source." [Online]. Available: <https://www.thorlabs.com/thorproduct.cfm?partnumber=OSL1>
- [30] "Named pipe." [Online]. Available: <https://docs.microsoft.com/en-us/windows/win32/ipc/named-pipes>
- [31] H.Fan, "Infrared hyperspectroscopy automated scanning user's guide."

- [32] V. Roberts, “Incoherent sources — lamps,” in *Encyclopedia of Modern Optics*, R. D. Guenther, Ed. Oxford: Elsevier, 2005, pp. 208–217.
[Online]. Available:
<https://www.sciencedirect.com/science/article/pii/B0123693950008551>
- [33] B. Das, “Obtaining wien’s displacement law from planck’s law of radiation,” *The Physics Teacher*, vol. 40, no. 3, pp. 148–149, 2002. [Online]. Available:
<https://doi.org/10.1119/1.1466547>
- [34] C. Elvidge, D. Keith, B. Tuttle, and K. Baugh, “Spectral identification of lighting type and character,” *Sensors (Basel, Switzerland)*, vol. 10, pp. 3961–88, 04 2010.